1 An evaluation of phase, aerosol-cloud interactions and microphysical properties of single- and

2 multi-layer clouds over the Southern Ocean using in situ observations from SOCRATES **John J.**

3 **D'Alessandro[1,2,*], Greg M. McFarquhar[1,2], Jeffrey L. Stith[3], Minghui Diao[4], Paul J.**

4 **DeMott[5], Christina S. McCluskey[6], Thomas C. J. Hill[5], Greg C. Roberts[7,8], Kevin J.**

5 **Sanchez[7]**

6 *[1]Cooperative Institute for Severe and High Impact Weather Research and Operations, University*

7 *of Oklahoma: Norman, OK, USA, 73072.*

8 *[2]School of Meteorology, University of Oklahoma, Norman, OK, USA 73072*

9 *[3]National Center for Atmospheric Research, Research Aviation Facility/Earth Observing*

10 *Laboratory: Boulder, CO, USA, 80307*

11 *[4]Department of Meteorology and Climate Science, San Jose State University, San Jose, CA,*

12 *USA, 95192*

13 *[5]Department of Atmospheric Science, Colorado State University, Fort Collins, CO, USA 80512*

14 *[6]Climate and Global Dynamics Laboratory, National Center for Atmospheric Science, Boulder,*

15 *CO, USA*

16 *[7]Scripps Institution of Oceanography, University of California in San Diego, La Jolla, USA*

17 *92093*

18 *[8]Centre National de Recherches Météorologiques, Université de Toulouse, Météo-France,*

19 *CNRS, Toulouse, France*

20 *[*]Current Affiliation: Department of Atmospheric Science, University of Washington, Seattle,*

21 *WA, USA, 98195*

22 Abstract

23 Single- and multi-layer clouds are commonly observed over the Southern Ocean in varying

24 synoptic settings, yet few studies have characterized and contrasted their properties. This study

25 provides a statistical analysis of the microphysical properties of single- and multi-layer clouds

26 using in-situ observations acquired during the Southern Ocean Cloud-Radiation Aerosol

27 Transport Experimental Study (SOCRATES).

28 The relative frequencies of ice-containing samples (i.e., mixed and ice phase) for multi-layer

29 clouds are 0.05 to 0.25 greater than for single-layer clouds, depending on cloud layer height. In

30 multi-layer clouds, the lowest cloud layers have the highest ice-containing sample frequencies,

31 which decrease with increasing cloud layer height up to the third highest cloud layer. This

32 suggests a prominent seeder-feeder mechanism over the region. Ice nucleating particle (cloud

33 condensation nuclei) concentrations are positively (negatively) correlated with ice-containing

34 sample frequencies in select cases.

35 Differences in microphysical properties are observed for single- and multi-layer clouds. Drop

36 concentrations (size distributions) are greater (narrower) for single-layer clouds compared with

37 the lowest multi-layer clouds. When differentiating cloud layers by top (single- and highest

38 multi-layer clouds) and non-top layers (underlying multi-layer clouds), total particle size

39 distributions (including liquid and ice) are similarly broader for non-top cloud layers.

40 Additionally, drop concentrations in coupled environments are approximately double those in

41 decoupled environments.

42 Significant findings:

43   -   The occurrence frequency of ice is greater in multi-layer clouds than in single-layer

44   clouds.

45   -   Drop number size distributions are broader in multi-layer clouds compared to single-layer

46   clouds.

47   -   Liquid drop number concentrations are approximately double in environments coupled

48   with the surface compared to decoupled environments.

49   1. Introduction

50   Clouds over the Southern Ocean have been notoriously difficult to simulate in both climate

51   models (e.g., D'Alessandro et al., 2019; Kay et al., 2012; Matus & L'Ecuyer, 2017; McCoy et

52   al., 2014) and high resolution models (Huang et al., 2014, 2015; Naud et al., 2014). Climate

53   models have overestimated shortwave absorption over this region (Trenberth & Fasullo, 2010),

54   which has been attributed to the underestimation of liquid water content and cloud fraction (e.g.,

55   Bodas-Salcedo et al., 2016). This may be due in part to extremely low ice nucleating particle

56   (INP) concentrations (N_{INP}) present over the Southern Ocean as observed from ships

57   (McCluskey et al., 2018). While recent model changes have improved simulated clouds with an

58   increased frequency of supercooled liquid, work is still required to further improve the

59   representation of microphysical properties (e.g., Fiddes et al., 2022; Gettelman et al., 2020;

60   McCoy et al., 2021; Yang et al., 2021) and the understanding of processes producing and

61   sustaining supercooled water.

62   Single- and multi-layer clouds are commonly observed over the Southern Ocean, with prior

63   observations indicating multi-layer clouds accounted for 34% of cases when clouds were present

64   (Haynes et al., 2011). Multi-layer clouds refer to the presence of multiple cloud layers separated

65   by a cloud free interstice, containing either precipitation or clear-sky (e.g., Intrieri et al., 2002;

66   Liu et al., 2012). This is distinct from vertically heterogeneous clouds, in which cloud properties

67   embedded within a single-cloud layer vary (e.g., Verlinde et al., 2013). Although climate models

68   often fail to capture multi-layer clouds due to their coarse vertical resolution (e.g., Atlas et al.,

69   2020), multi-layer clouds occur frequently and substantially impact the radiative budget. Because

70   of this, climate models often parameterize vertical cloud overlap to adequately treat radiative

71   fluxes throughout vertical columns (e.g., Collins, 2001).

72   Although the reasons that multi-layer clouds form is still uncertain, multiple explanations have

73   been proposed. For example, Tsay & Jayaweera (1984) found that a combination of large-scale

74   processes can account for multi-layered stratus. Herman & Goody (1976) showed that shortwave

75   absorption by droplets within a cloud layer leads to evaporation within the cloud deck, which

76   along with destabilization due to longwave cooling at cloud top can lead to the formation of two

77   layers. Multiple cloud layers can also result from inhomogeneous temperature/moisture

78   horizontal advection (Luo et al., 2008). They are also associated with additional complexities

79   which do not need to be considered for single-layer regimes, such as seeder-feeder mechanisms

80   (e.g., Fleishauer et al., 2002; Hobbs & Rangno, 1998; Houze, 2014).

81   Differences in cloud layering can impact the zonally averaged top-of-atmosphere longwave and

82   shortwave radiative fluxes by the order of 10 W m^{-2} (Li et al., 2011), attributed in part to

83   differences in the cloud layer heights and thicknesses. Further, overlying cloud layers can

84   substantially impact the evolution of the underlying boundary layer clouds. Their presence

85   increases downward longwave radiative flux by an average of 30 W m^{-2}, impacting turbulent

86   mixing, vertical development and precipitation rates of the underlying cloud layers (Christensen

87   et al., 2013).

88   Cloud layer microphysical properties substantially impact turbulent, precipitation and radiative

89   properties. Thus, high vertical resolution measurements of cloud profiles are needed for both

90   single- and multi-layer clouds. A few studies showing vertical profiles of cloud microphysical

91   properties over the Southern Ocean using in situ observations have been performed (e.g., Ahn et

92   al., 2017, 2018; Boers et al., 1996, 1998; Chubb et al., 2016; Chubb et al., 2013). However, they

93   were primarily case studies lacking statistically significant datasets, and they primarily focused

94   on single-layer clouds. Little effort has been put towards contrasting the microphysical properties

95   of single-versus multi-layer clouds, and the dearth of prior in situ observations over the Southern

96   Ocean relative to the Arctic warrants a statistical analysis of the varying properties of single- and

97   multi-layer clouds. Further, satellite observations are often restricted to cloud top (Coopman et

98   al., 2020; Riedi et al., 2010), and there are uncertainties with low-level cloud retrievals due to

99   attenuation (Hu et al., 2009) and low solar zenith angles (Khanal & Wang, 2018). For these

100   reasons, in situ observations can be extremely beneficial towards analyzing both low-level cloud

101   layers as well as multi-layered clouds commonly observed over this region.

102   This study aims to produce a statistical overview of single- and multi-layer clouds over the

103   Southern Ocean using in situ observations. It extends the study of Schima et al. (2022) who used

104   a combination of in-situ and remote sensing data to identify common features of the vertical

105   cloud structure over the Southern Ocean, but who did not stratify clouds into single- or multi-

106   layers, and who did not examine how cloud properties varied with the concentration of ice

107   nucleating particles (INPs) or cloud condensation nuclei (CCN). The following section will

108   describe the instrumentation and the methodology used to obtain vertical profiles as well as

109   classify the measured profiles as either single- or multi-layer clouds. Section 3 presents the cloud

110   microphysical properties and phase occurrence frequencies for single- and multi-layer clouds, as

5

111   well as comparisons of cloud condensation nuclei (CCN) and INP in relation to cloud properties.

112   Section 4 discusses the significance of the results presented in Section 3, and Section 5 delivers

113   concluding remarks.

114   2. Methodology

115   2.1: Instrumentation and cloud presence/phase methodology

116   This study uses observations acquired with instruments onboard the National Science

117   Foundation/National Center for Atmospheric Research Gulfstream-V (G-V) aircraft during the

118   Southern Ocean Cloud-Radiation Aerosol Transport Experimental Study (SOCRATES).

119   SOCRATES was based out of Hobart, Tasmania and consisted of 15 research flights.

120   SOCRATES took place from 15 January to 28 February 2018, sampling the atmosphere over the

121   Southern Ocean from 42° to 62°S and from 133° to 163°W. Flight plans were designed to ideally

122   sample 10-minute level legs above cloud, in cloud, and below cloud, followed by sawtooth legs

123   (i.e., sawtooths) to obtain vertical profiles. A variety of synoptic conditions occurred during the

124   campaign, including the passage of multiple extra tropical cyclones as well as an atmospheric

125   river (1/28/2018, Finlon et al., 2020; Rauber et al., 2020). The aircraft primarily targeted cold

126   sector boundary layer clouds, although regions of both synoptic ascent and descent were

127   commonly sampled. Prevailing winds were primarily westerly and southwesterly. Additional

128   details on synoptic conditions, flight objectives and analyses can be found in McFarquhar et al.

129   (2021).

130   A suite of cloud probes and other instrumentation was installed on the G-V. The cloud droplet

131   probe (CDP) is a single-scatter particle probe which gives information of cloud particle size

132   distributions for particles with maximum dimension (hereafter size D) ranging from 2–50 μm.

133 Because the CDP sizes particles assuming Mie theory which corresponds to diameters of

134 spherical particles, there are large uncertainties in the derived particle sizes and mass contents for

135 ice clouds. The two-dimensional stereo probe (2DS) is an optical imaging array probe with a

136 photodiode array having a resolution of 10 μm from which particle number size distribution

137 information can be derived. Although the width of the photodiode array of the 2DS corresponds

138 to particles with maximum dimensions ranging from 10 to 1280 μm, only particles having

139 maximum dimension (D_{2DS}) greater than or equal to 50 μm were included in the derived particle

140 number size distributions because of its small and highly uncertain depth of field for $D_{2DS} < 50$

141 μm (e.g., Baumgardner & Korolev, 1997). The SOCRATES 2DS size distributions and particle

142 morphological data (Wu & McFarquhar, 2019) were determined using the University of

143 Illinois/Oklahoma Optical Probe Processing Software (UIOOPS; McFarquhar et al., 2018;

144 McFarquhar et al., 2017), and include corrections for removal of shattered artifacts (Field et al.,

145 2003, 2006). Particles larger than the width of the photodiode array are included due to the use of

146 particle reconstruction provided the particle center occurs within the array (Heymsfield &

147 Parrish, 1978). Mass distribution functions are determined using the habit-dependent mass-size

148 relationships summarized by Jackson et al. (2012, 2014) for the different particle habits that are

149 identified in UIOOPS (McFarquhar et al., 2018) following a modified Holroyd (1987) approach.

150 Hereafter, bulk properties of cloud particles measured by the CDP and 2DS correspond with the

151 properties of cloud particles with D less than and greater than 50 μm, respectively.

152 Samples are determined to be either in-cloud or clear-sky following D'Alessandro et al. (2021),

153 which utilizes measurements from the CDP and 2DS. Samples are considered in-cloud if the

154 derived mass content of CDP observations (M_{CDP}) is greater than 10^{-3} g m^{-3} or if any particles are

155 detected with $D_{2DS} > 50$ μm. These threshold values were selected to eliminate sea spray and other

156 large aerosols. The low threshold of M_{CDP} ensures that even optically thin clouds are included in

157 the sample. The phase of in-cloud samples is also determined following D'Alessandro et al.

158 (2021), which determines the phase of small cloud particles (D<50 μm) using a set of threshold

159 values for the CDP and Rosemount Icing Detector measurements, whereas the phase of large

160 particles (D>50 μm) uses a combination of multinomial logistic regression and visual

161 examination of particle imagery from the 2DS. The phase of large particles may be classified as

162 either liquid, ice or mixed (i.e., a sample volume containing both liquid and ice particles)

163 whereas the phase of small particles may only be classified as either liquid or ice. Number

164 concentrations of the CDP (N_{CDP}) greater than 10 cm^{-3} are generally liquid samples

165 (D'Alessandro et al., 2021; Finlon et al., 2019; Heymsfield et al., 2011; Lance et al., 2010).

166 Additional information of the phase classification and associated uncertainties can be found in

167 D'Alessandro et al. (2021).

168 Additional instrumentation to obtain measurements utilized in this study are described below.

169 Filters were collected using a forward-facing inlet (Stith et al., 2009) on the G-V for offline

170 immersion freezing measurements. INP number concentrations were determined from particles

171 collected onto the filters and released into suspensions that were analyzed using the Colorado

172 State University ice spectrometer (DeMott et al., 2017). The INP filter sample collection and

173 analysis approach similarly follows that of previous aircraft studies (Levin et al., 2019; Twohy et

174 al., 2016), wherein further details on the methodology can be found. Measurements of CCN were

175 obtained using two miniaturized stream-wise thermal gradient CCN counters (Roberts & Nenes,

176 2005; Sanchez et al., 2021). One gathered 1 Hz data at a constant supersaturation of 0.43%,

177 while the other operated with a scanning flow and temperature to measure CCN spectra from

178 0.06% to 0.87% supersaturation every five minutes. This study uses measurements from the

179   latter, but only CCN data with supersaturations between 0.26% to 0.34%. This range of

180   supersaturation is chosen since CCN concentrations at this are similar to observed N_{CDP}

181   concentrations (Sanchez et al., 2021). Shortwave irradiance measurements were taken with a

182   Kipp and Zonen CMP22 Pyranometer. Infrared irradiance measurements were taken using two

183   Kipp and Zonen CGR4 Pyrgeometers. Temperature was measured using a fast-response

184   Rosemount temperature probe. For steady conditions the estimated accuracy and precision are

185   0.3K and 0.01K, respectively. Water vapor was measured using the 25-Hz Vertical Cavity

186   Surface Emitting Laser (VCSEL) hygrometer (Zondlo et al., 2010). Additional laboratory

187   calibrations of the VCSEL water vapor measurements were conducted in summer 2018, and the

188   final data were reprocessed (Diao, 2021). Relative humidity (RH) is calculated following

189   Murphy & Koop (2005). The combined uncertainties from temperature and water vapor

190   measurements results in the uncertainty of RH ranging from 6.3%–6.7% from 17° to -31°C,

191   respectively, which is the temperature range of the cloud layers in this study (discussed in more

192   detail in the following section). Vertical air motion was measured with the Radome Gust Probe

193   in combination with pitot tubes and the differential Global Positioning System. Cooper et al.

194   (2016) reports a net uncertainty in the standard measurements of vertical wind measurements to

195   be 0.12 m s^{-1}, although this represents ideal sampling conditions. Additional information on the

196   G-V gust probe performance and processing is provided in the manager's report (EOL, 2018;

197   https://www.eol.ucar.edu/system/files/SOCRATES%20PM%20Report.pdf). Remote sensing

198   platforms onboard the aircraft include the High-performance Instrumented Platform for

199   Environmental Research (HIAPER) Cloud Radar (Vivekanandan et al., 2015) and High Spectral

200   Resolution Lidar (Eloranta, 2006).

201   2.2: Cloud layer classification

202   Clouds measured during all sawtooth maneuvers, ascents and descents during SOCRATES are

203   classified as either single- or multi-layer clouds. In the analysis, transects are first defined as

204   ascending or descending legs, and included in the analysis provided the rate of altitude change

205   was consistently greater than 3 m s^{-1} for the transect. The typical ascent or descent rate of the G-

206   V during sawtooths was 5 to 7.5 m s^{-1}. Transects with vertical lengths less than 60 m are

207   removed from this analysis, all of which only contained one single-cloud layer. Level legs are

208   not included in the analysis because they do not provide information about the vertical profile.

209   An automated cloud layer classification method is introduced to provide an objective measure

210   for identifying individual layers within each transect. For data obtained during each transect, a

211   smoothing filter is applied to all 1-s in-cloud samples defined as having $M_{CDP} > 10^{-3}$ g m^{-3}. A

212   binary array is first created (a cloud flag) where samples with $M_{CDP} > 10^{-3}$ g m^{-3} are set equal to

213   one and all other samples equal to 0. A Savitzky-Golay smoothing method (Savitzky & Golay,

214   1964) is applied with a moving window of 30 1-Hz samples to each binary array. The Savitzky-

215   Golay filter is used since it better preserves peak heights and widths of data features compared

216   with lower order moving averages. Individual layers are identified where consecutive samples of

217   the smoothed binary arrays exceed 0.5. Clear interstices between layers on the order of meters

218   can potentially be captured using this method, with the exact threshold dependent on the aircraft

219   rate of ascent or descent. The smallest distance between layers found here was 30 m. The vertical

220   extent of the cloud layer within an area where the smoothed binary array exceeds 0.5 is

221   determined to be between the highest and lowest in-cloud sample having $M_{CDP} > 10^{-2}$ g m^{-3}. The

222   lower M_{CDP} threshold applied prior to smoothing ensures cloud top and base is contained in each

223   area of the smoothed binary area exceeding 0.5. All layers identified using this method are

224   shown by the shaded rectangles in Figure 1. The CDP is solely used to identify cloud layers

10

225 without the use of the 2DS to ensure that the presence of precipitating ice or drizzle is not used to

226 identify a cloud layer when small droplets or ice crystals are not present. A cloud layer is only

227 included in the analysis if the entirety of the layer (cloud base to cloud top) is contained within

228 the transect. Sensitivity tests were performed to determine how cloud top and base changed when

229 the mass threshold was decreased to 10^{-3} g m^{-3} and increased to 0.05 g m^{-3} (not shown).

230 Although the lower (higher) threshold increased (decreased) the total number of cloud layer

231 samples by ~5% (~8%), the trends presented in the manuscript do not change regardless of the

232 threshold used.

233 Although flight plans were designed with the intent of sampling all cloud layers during sawtooth

234 maneuvers, it is possible that some layers were missed if the G-V did not ascend or descend to

235 the altitude where these layers were located. Furthermore, for transects where there was a very

236 narrow interstice between layers, the irregular clustering of CDP measurements make it difficult

237 to determine the number of layers. Thus, the G-V forward-facing camera was inspected for each

238 transect to evaluate the classification. This was additionally required for cases when the G-V

239 intersected the same cloud layer twice (e.g., protruding filaments of cloud below cloud base).

240 Reflectivity profiles from the HIAPER cloud radar and retrievals from the HSRL acquired

241 during the transects were similarly used to distinguish cloud layers and check for cloud layers

242 directly above and below the aircraft. Manual inspection of the layer classification resulted in

243 16% of the layers requiring correction.

244 Figure 1 shows M_{CDP} from vertical transects flown by the G-V aircraft, with layers indicated by

245 the coloring within each rectangular box. Each column represents a single-vertical transect,

246 arranged in the order they took place as shown by the research flight number (RF01–RF15)

247 underlying the respective columns. The color of the rectangular box surrounding the M_{CDP}

248   shading represents the identification of that profile as either a single-layer, or the lowest (Multi-

249   1st), second lowest (Multi-2nd), third lowest (Multi-3rd) or higher layer (Multi-grt3rd) in a

250   multi-layer cloud as determined from the cloud layer classification. Both single- and multi-layer

251   clouds were regularly encountered in approximately half the flights, whereas other flights

252   predominantly sampled either multi-layer or single-layer clouds (e.g., RF01 only has two-layer

253   clouds, RF12&13 primarily have single-layer clouds). The magnified panel in Figure 1 shows

254   profiles representative of most of the layers sampled and includes phase information as colored

255   markers immediately to the right of the transects. Cloud layers were typically composed of

256   supercooled liquid and mixed phase samples. A case of light ice precipitation (M_{2DS}<0.01 g m^{-3})

257   is observed for the highest cloud layer in the middle transect, indicated by the blue phase

258   markers immediately to the right and underlying the top cloud layer. Cloud layers were often

259   found to precipitate either supercooled drizzle or ice, which has been previously documented

260   (Alexander et al., 2021; Schima et al. 2022). Overall, 55 single-layer clouds and 183 multi-layer

261   clouds were identified from 153 transects using this procedure. Only 63% of the cloud layers

262   obtained through the layer classification are shown in Figure 1, since Figure 1 only shows cloud

263   layers from transects which do not have an in-cloud sample at the highest nor lowest point.

264   Although cloud layers are included in the analysis regardless of their altitude, the vast majority

265   of sampling took place below 3 km (96% of single-layer clouds and 98% of multi-layer clouds).

266   Since M_{CDP} is solely used to determine in-cloud conditions, the cloud layer classification method

267   fails to capture ice cloud layers with M_{CDP} below the in-cloud threshold. One such layer is in the

268   magnified panel of Figure 1 as seen by the presence of M_{2DS}>0.01 g m^{-3} (black shading and blue

269   markers). Note that the phase information is only visible for approximately half the length of the

270   layer since temperatures exceed 0°C below the markers and phase information is only provided

271   for temperatures less than 0°C. There were six such layers in total (2% of the observed layers),

272   which are not included in the analysis to be consistent with the in-cloud definition ($M_{CDP} > 10^{-3}$ g

273   m^{-3}) proposed to exclude precipitating particles. Additionally, the cloud layer classification

274   method may fail to accurately capture cloud layers which contain these ice layers embedded

275   within multiple liquid or mixed phase layers. However, there were only three such layers (1% of

276   the layers) embedded with multiple liquid layers as well as ice layers which were deep enough to

277   prevent the smoothing algorithm from adequately classify the cloud layers. These layers were not

278   included in the analysis.

279   3. Results

280   3.1: Cloud layer overview

281   Figure 2 shows the number of profiles with different layer depths (i.e., geometric thickness) for

282   the single- and multi-layered cases (Figure 2A), as well as the normalized occurrence frequency

283   of different phases that occur in single-layer and multi-layer clouds (Figure 2B). The number of

284   Multi-2nd layers (70) is greater than the number of Multi-1st (64) layers because every sawtooth

285   does not necessarily capture every cloud layer within a given atmospheric profile. Figure 2A

286   shows that relatively thin cloud layers with depths < 200 m are more frequent than deeper layers

287   for both single-layer and multi-layer clouds, and for all different layers of the multi-layer clouds,

288   with these thin cloud layers representing 59% of the layers sampled during SOCRATES. Cloud

289   layers with average temperatures less than 0°C make up 76% of all the layers sampled, with 63%

290   of all such layers having depths < 200 m. Here cloud layers above and within the boundary layer

291   are explored separately due to inherent differences in air properties and aerosol profiles at these

292   heights. Approximately 72% of the multi-layer clouds were observed within the boundary layer

293   and 28% above the boundary layer, and approximately 70% of single layer clouds were observed

294   within the boundary layer. The boundary layer heights were determined from dropsonde data

295   using a maximum gradient method developed by Hande et al., (2012) where boundary layer

296   heights are determined as the altitude where the maximum gradient of virtual potential

297   temperature occurs. The range of possible heights is restricted to 100 m and 2500 m, and the

298   virtual potential temperature is smoothed with a five-point moving average. Other methods have

299   been proposed for determining boundary layer heights using alternative gradient methods

300   utilizing other parameters (e.g., Engeln & Teixeira, 2013) or using a bulk Richardson number

301   (Seidel et al., 2012; Vogelezang & Holtslag, 1996) where the boundary layer height is the lowest

302   altitude where the bulk Richardson number exceeds 0.25. From visual inspection, it was

303   determined that the maximum gradient method produces better estimates of the boundary layer

304   height than the bulk Richardson method, possibly because the Richardson method is only a

305   measure of local turbulence, which may not be suitable for convective boundary layers. The

306   mean and median boundary layer heights using the maximum gradient method are both ~1450 m

307   with a standard deviation of 510 m. For flights without dropsonde data (dates 1/15,2/3,2/4),

308   boundary layer heights are estimated via visual inspection from in situ temperature

309   measurements acquired during sawtooths. Finally, boundary layer heights are interpolated using

310   a nearest neighbor method over each respective flight. Some layers could therefore be incorrectly

311   characterized as either above or within the boundary layer based on uncertainties or limitations

312   associated with the interpolation method.

313   Figure 2B shows that single-layer clouds contain the smallest percentage of ice-containing

314   samples (6%), where ice-containing samples are either ice-phase or mixed-phase clouds, whereas

315   the lowest layers of multi-layer clouds have the highest observed frequency of ice-containing

316   phases (32%). The frequency incrementally decreases with increasing multi-layer cloud height

14

317   up to the third lowest cloud layer. The highest layers of multi-layer clouds have nearly similar

318   frequencies of ice-containing samples (31%) as the lowest layers. The phase frequencies are

319   separately analyzed for above and within the boundary layer (not shown), and the trends

320   discussed above are observed in both cases (i.e., greatest liquid phase frequencies in single layer

321   clouds, lowest liquid phase frequencies in lowest multi-layer clouds and increasing liquid phase

322   frequencies up to the third highest cloud layers). Frequency values within the boundary layer are

323   all within 10% of those in Figure 2B, whereas values are much more variable above the

324   boundary layer. The fraction of samples that are mixed-phase compared to all ice containing

325   samples is greatest for single-layer clouds, with slightly lower frequencies for multi-layer clouds,

326   with the frequency decreasing with increasing cloud height (blue text within respective columns

327   of Figure 2B). Within all cloud layers, over 95% of ice-containing samples are mixed-phase

328   showing the dominance of supercooled water regardless of layering.

329   The vertical distances and properties between the layers of multi-layer clouds are also explored

330   in an effort to document differences in dynamical and precipitation characteristics. The

331   frequency distribution of distances between cloud layers is shown in Figure 3A. The distances

332   are skewed to the left, with approximately half less than 200 m and a median distance of 209 m.

333   A wide variety of synoptic conditions were sampled during SOCRATES, with winds primarily

334   westerly (~270°) or southwesterly (~220°). Figure 3B shows that winds were primarily

335   southwesterly for closely-residing cloud layers (i.e., distance between layers less than 200 m),

336   whereas they were primarily westerly for other multi-layer clouds, suggesting a dynamical link

337   for multi-layer clouds with varying distances in-between the layers.

338   Normalized frequency distributions of relative humidity between cloud layers in Figure 3C show

339   the air was often nearly saturated between all cloud layers, with peak occurrence frequencies of

340   90% to 95%. These peaks are greater for closely-residing cloud layers (~0.2) compared with

341   layers further apart (~0.1). To explore whether this is related to the presence of in-cloud samples

342   within the layers, clear-sky frequencies (number of clear-sky samples to all samples) and liquid

343   phase frequencies (number of liquid phase samples to all phases) are shown in Figure 3D for

344   temperatures from -20° to 0°C, which contained 99% of samples for depths less than 200 m and

345   95% for depths greater than 200 m. To determine the fraction of in-cloud samples that are

346   precipitating, the clear-sky and liquid phase frequencies are computed using only in-cloud

347   samples that contain particles with D > 50 μm. The clear-sky frequencies vary from ~0.7–0.95

348   for depths exceeding 200 m and 0.4–0.7 for depths less than 200 m. The relatively high clear-sky

349   frequencies may not necessarily indicate the top cloud layer never was precipitating, since the

350   aircraft may have penetrated the layers after the event. However, the clear-sky frequencies are

351   lowest from -5° to 0°C for closely-residing cloud layers, with over half of the samples within the

352   layers associated with precipitation. This is also the temperature range which contains half of all

353   closely-residing cloud layer samples.

354   The liquid phase frequencies of the precipitating samples vary from 0.25–0.75 for depths less

355   than 200 m and 0.05–0.45 for depths exceeding 200 m. The lowest liquid phase frequencies are

356   observed in the highest temperature bin consistent with precipitating ice beneath liquid topped

357   cloud layers. The liquid phase frequency from -20° to 0°C for both depth ranges is

358   approximately 0.32, highlighting a higher frequency of ice-containing samples relative to liquid-

359   only samples.

360   3.2.1: INP related to cloud phase

361   Determining the concentration of INP over the SO is difficult in part due to their relatively sparse

362   concentrations over the region (McCluskey et al., 2018; McFarquhar et al., 2021), which means

363   long averaging times are required to get statistically significant samples. The following

364   discussion provides context for the INP observations gathered from the G-V aircraft during

365   SOCRATES and used in this analysis. It is worth noting that these observations are the first

366   airborne INP measurements taken over the Southern Ocean region. Sampling of INP is taken

367   over continuous durations on the order of minutes, which here are defined as sample areas. To

368   accommodate the low aerosol loadings over the Southern Ocean, filters were collected during

369   periods (i.e., within given sample areas) of clear-air that were representative of the below-cloud

370   layer, above-cloud layer and in the free troposphere. The sample areas were often combined in

371   post-campaign processing accounting for flow rates which ranged from a few to 13 liters per

372   minute (depending on altitude). Sample areas above and within the boundary layer were

373   separately combined, with the combined areas spanning up to 15° latitude. This resulted in

374   accumulated sample volumes ranging from 129 to 840 standard liters of air per flight. The total

375   data acquisition time of all samples amounts to approximately 23 hours, with a total of 32 filter

376   samples obtained. Since the reported activation temperatures vary for different combined sample

377   areas, reported N_{INP} are averaged at 1°C intervals to obtain N_{INP} with a constant activation

378   temperature resolution of 1°C.

379   The following analysis relates N_{INP} with relative phase frequencies. To obtain adequate cloud

380   phase sample size(s), combined INP sample areas are interpolated using a nearest neighbor

381   method over the respective flights. Cloud phase data within the interpolated sample areas

382   (including sawtooth and level-leg data) is then related to N_{INP} from the same sample area(s). The

383   interpolation is separately performed for sample areas above the boundary layer and within the

384   boundary. This mostly results in interpolated sample areas derived from single sample areas

385   above and within the boundary layer spanning the entire research flights, with the exception of

386 research flights 1,3,4,10. Namely, with the exception of the research flights listed, all in-cloud

387 data above (within) the boundary layer is related with a single set of reported N_{INP} above (within)

388 the boundary layer.

389 Scatterplots relating N_{INP} and liquid phase frequency are shown in Figure 4. Results are

390 separately shown within the boundary layer (Figure 4A) and above the boundary layer (Figure

391 4B). The different colored markers denote cases where the liquid phase frequency is taken within

392 a specified temperature range (left-hand side of legend text) located within a given interpolated

393 sample area and relates it to N_{INP} having activation temperatures within a specified range (right-

394 hand side of legend text) associated with the same interpolated sample area. The N_{INP} values

395 over the specified activation temperature ranges are the sums of the averaged N_{INP} values

396 determined for the constant 1°C activation temperature bins. Measurements of INP are reported

397 with activation temperatures ranging from -30° to -10°C, noting N_{INP} is only measurable for

398 activation temperatures <-10°C. Phase data for temperatures below -20°C are not included

399 because D'Alessandro et al. (2021) previously showed there is a sharp decrease in supercooled

400 liquid below -20°C, with ~93% of samples between -30° and -20°C being ice phase. Strong

401 negative relationships would likely indicate a prevalence of primary nucleation over the region.

402 Perhaps the most likely temperature range and N_{INP} activation temperature range expected to

403 show such relationships would be those having similar ranges. However, data points representing

404 liquid phase frequencies from -20° to -10°C and N_{INP} with activation temperatures in the same

405 range (red points) are associated with low sample sizes (i.e., number of in-cloud samples). This

406 is observed with only three data points within the boundary layer, and seven above the boundary

407 layer (three of which have sample sizes less than 200; denoted by marker size). This is due in

408 part to the fact that the number of in-cloud samples from -10° to 0°C is more than a factor of two

18

409   greater than the number of samples from -20° to -10°C (D'Alessandro et al., 2021); N_{INP} have

410   their lowest concentrations at relatively higher activation temperatures which increase semi-

411   exponentially with decreasing activation temperatures (Järvinen et al., 2022).

412   There are a few N_{INP} ranges which capture negative relationships between liquid phase frequency

413   and N_{INP} associated with primary nucleation. One is for N_{INP} with activation temperatures from -

414   30° to -10°C within the boundary layer, where the correlation between N_{INP} and liquid phase

415   frequencies from -20° to -2°C is -0.41. This negative correlation may be related to the fact that

416   INP measurements below -20°C are more reliable, and thus may better reflect N_{INP} having higher

417   activation temperatures. The correlation is similar (-0.51 to -0.41) when decreasing the range of

418   activation temperatures towards those greater than -30°C, until activation temperatures exceed -

419   25°C (not shown). However, this negative correlation is only observed within the boundary

420   layer, which is unexpected since there were no in-cloud samples obtained below -20°C within

421   the boundary layer. Therefore, the correlation may be related to sedimenting INP from above the

422   boundary layer even though there is no notable relationship between similar N_{INP} and liquid

423   phase frequency temperature ranges above the boundary layer. One possible explanation for this

424   observation may be the prominence of efficient ice nucleation due to pre-activated INP (Mossop,

425   1956), whereby localized regions above the boundary layer may only experience significant

426   primary nucleation via pre-activated INP. Thus, primary ice nucleation may occur at lower

427   temperatures above the boundary layer, and contributions from alternative processes such as

428   accretion and seeding mechanisms may decrease liquid phase frequencies at higher temperatures

429   underlying the localized areas. There is indirect evidence for this when relating N_{INP} above the

430   boundary layer with phase frequencies within the boundary layer (Figure 4B; purple circles).

431   This is done by obtaining the phase frequencies below the boundary layer using the above

432   boundary layer interpolated sample areas. A correlation of -0.96 is observed between N_{INP} with

433   activation temperatures from -30° to -20°C and phase frequencies from -20° to -7°C for

434   datapoints exceeding 200 samples, and a correlation of -0.87 is observed by removing the only

435   datapoint with less than 200 samples having a liquid phase frequency of ~0.5. This finding is not

436   directly indicative of a significant contribution from pre-activated INP, as results may also be

437   indicative of a seeding mechanism resulting from INP which are not pre-activated. Further, it is

438   important to note that to the authors' knowledge there are no prevailing studies which similarly

439   suggest the importance of pre-activated INP in any region globally.

440   All the other N_{INP} ranges are weakly correlated with liquid phase frequency ($|r|<0.2$), with the

441   exception of N_{INP} with activation temperatures from -20° to -10°C and liquid phase frequencies

442   within the same temperature range within the boundary layer, although this dataset only contains

443   three points. Aside from select combinations of N_{INP} and phase frequencies discussed above,

444   there are no clear relationships between most combinations of the listed phase frequencies and

445   N_{INP}, suggesting a prominence of alternative ice initiation/growth processes (secondary ice

446   nucleation, accretion, etc.). Relationships may be sensitive to whether INP sampling took place

447   above or below clouds, although it is at best extremely difficult to incorporate this distinction due

448   to the interpolated sampling area method discussed above. Additionally, results may be sensitive

449   to the fact that N_{INP} values in Figure 4 are biased towards reported N_{INP} at the lowest end of their

450   respective activation temperature ranges, due to the semi-exponential increase in reported N_{INP}

451   with decreasing activation temperatures. At the very least, results here provide a benchmark

452   analysis towards directly relating INP to the frequency of ice over the Southern Ocean.

453   3.2.2. CCN related to cloud phase

454   Liquid phase frequencies are also related to CCN number concentrations (N_{CCN}) to determine the

455   potential impacts of CCN on cloud phase. Due to the greater spatial resolution of CCN

456   measurements compared with INP sample areas, a method is derived to obtain a CCN number

457   concentration associated with each cloud sample. Since droplet shattering on the community

458   aerosol inlet of the CCN counter introduces error in its measurements (Hudson & Frisbie, 1991),

459   CCN measurements cannot be used within in-cloud samples. To avoid such errors, suitable CCN

460   concentration measurements (hereafter referred to as N_{CCN}) are determined using a moving

461   window ± n seconds (n ranges from 100 to 500 seconds) from each cloud sample. Within this

462   window, the average N_{CCN} is calculated only using clear-sky samples. The averaging method is

463   also restricted to samples above or within the boundary layer, depending on the location of the

464   in-cloud sample. Thus, each in-cloud sample is associated with a "background CCN

465   concentration" value based on the moving window average. Results applying this methodology

466   are shown in Figure 5, showing the liquid phase frequency for different temperature ranges

467   (where temperature values are used at the in-cloud location) above the boundary layer (5A–C)

468   and within the boundary layer (5D–F). The different color lines denote the liquid phase

469   frequencies for different terciles of N_{CCN}, where the red line denotes samples in the lower tercile,

470   the black line in the middle tercile and the blue line in the upper tercile. Terciles are determined

471   within the respective temperature bins, whereas terciles determined over the entire temperature

472   range (-20° to 0°C) are shown in the respective panels. Each column shows results using a

473   different moving average window size (100, 250 and 500 seconds), shown overlying the

474   respective columns. Results are relatively consistent over the different window sizes but not

475   location. Within the boundary layer, liquid phase frequencies are either relatively constant or

476   slightly increase with decreasing temperature for all the moving window sizes (5D–F). The

477   possible exception is the lower tercile at smaller windows, with an initially low liquid phase

478   frequency from -10° to -5°C which increases with increasing window size as the sample size

479   increases. Although inconsistent with observed increases in the frequency of ice-containing

480   cloud samples with decreasing temperatures (D'Alessandro et al., 2021), results here are

481   consistent with the increasing liquid phase frequencies with increasing cloud height (Figure 2B).

482   In contrast, most liquid phase frequencies generally decrease with temperature over all the CCN

483   percentiles above the boundary layer (5A–C). Stark contrasts in the liquid phase frequencies

484   above the boundary layer are observed for the different CCN percentiles which were not

485   observed within the boundary layer. Namely, liquid phase frequencies are much greater within

486   high N_{CCN} environments than low N_{CCN} environments at temperatures less than -10°C. In fact,

487   with the exception of one temperature bin (from -10° to -5°C for the ±100 s window; 5A), the

488   liquid phase frequencies in the high N_{CCN} environments are greater than the low N_{CCN}

489   environments for all temperatures and moving window sizes. Liquid phase frequencies for the

490   middle tercile do not always lie between the upper and lower terciles, and are often closer to

491   frequencies of the lower terciles at temperatures less than -10°C. This suggests relatively high

492   CCN perturbations may be required to maintain the absence of ice at these relatively lower

493   temperatures. Previous studies have found high N_{CCN} environments correspond with increased

494   frequencies of supercooled liquid in low-level Arctic clouds, which has been suggested to be due

495   to increasing lifetimes of supercooled liquid clouds (Filioglou et al., 2019). Alternatively,

496   varying N_{CCN} environments may be representative of different air mass source regions, and

497   differences in phase frequencies may be the result of the different aerosol sources. Sanchez et al.

498   (2021) identified four aerosol regimes sampled during SOCRATES, and found environments

499   with high N_{CCN} commonly originated or passed over the Antarctic coast, where elevated

500   phytoplankton biomass (relative to the open ocean) is a major contributor of biogenic emissions

501   (Sanchez et al., 2016). Additional explanation(s) may be related to varying secondary ice

502   production mechanisms related to the presence of large droplets, which would be limited in a

503   high N_{CCN} environment. For example, drops having maximum dimensions exceeding ~50 μm

504   have been observed to eject small ice particles as they freeze (i.e., droplet fragmentation),

505   primarily at temperatures less than -10°C (Korolev & Leisner, 2020). However, Järvinen et al.

506   (2022) found little evidence to suggest this is a prominent secondary ice production mechanism

507   over the SOCRATES region. A more prominent mechanism is referred to as the Hallett-Mossop

508   process, which is characterized by splintering of small ice particles off of graupel during riming

509   (Hallett & Mossop, 1974). Previous studies have noted its likely presence over the Southern

510   Ocean (Huang et al., 2021; Järvinen et al., 2022), although this process is primarily restricted to

511   temperatures from -8° to -3°C where the greatest liquid phase frequency differences are not

512   observed.

513   An analysis comparing differences in drop concentrations in decoupled and coupled

514   environments is provided in Figure 6. Results separated in this manner can provide insight into

515   how surface-sourced parameters impact drop concentrations (e.g., sea spray acting as CCN).

516   Most of the boundary layers were decoupled with the exception of RF12 and RF13, where the

517   presence of coupling was determined using the dropsonde data following (Wang et al., 2016).

518   Figure 6 shows a distinct bimodality in N_{CDP} due to differences of N_{CDP} in the coupled and

519   decoupled environments. The mode of N_{CDP} for decoupled flights is 70 cm^{-3} and for coupled

520   flights 160 cm^{-3}, consistent with high aerosol number concentrations emitted from the ocean

521   serving as effective CCN in the coupled cases. Perhaps unexpectedly, average N_{CCN} within the

522   boundary layer is not the highest for either of the coupled research flights, but rather is highest

523   for RF09 (191 cm^{-3}), second highest for RF12 (175 cm^{-3}) and the third highest for RF13 and

524   RF08 (both are 136 cm^{-3}). Furthermore, average N_{CCN} for RF12&13 above the boundary layer

525   were the fifth and sixth highest of all 15 research flights. The tendency for RF12&13 not having

526   the highest average N_{CCN} is similarly observed when evaluating N_{CCN} at supersaturations greater

527   than and less than 0.3% (not shown). This is indicative of higher updraft speeds associated with

528   these two flights, which is consistent with a less kurtotic distribution of vertical air motions

529   (kurtosis=4.2) observed for in-cloud observations from these flights compared to the other

530   research flights (kurtosis=10.3; not shown). Note that kurtosis is used to capture the tail ends of

531   distributions (greater updraft and downdraft speeds) rather than skewness which may not capture

532   the greater updraft speeds if greater downdraft speeds are also present. However, Sanchez et al.

533   (2021) suggested that recent particle formation above the boundary layer and particle

534   growth/processing within the boundary layer are the primary source(s) of CCN in this region.

535   Alternatively, lower drop concentrations associated with decoupled flights could be related to

536   greater entrainment-mixing or precipitation scavenging.

537   3.3: Cloud layer properties and profiles of radiative fluxes and drop clustering

538   Figure 7 shows normalized frequency distributions of N_{CDP}, M_{CDP}, the standard deviation of D

539   from CDP drop size distributions (σ_{CDP}) and the mean volume weighted diameter (MVD_{CDP}) for

540   single-layer clouds and the different layers of multi-layer clouds using data from all flights. In

541   Figure 7A it is seen that the N_{CDP} mode for single-layer clouds is greater than 10^2 cm^{-3},

542   coinciding with the N_{CDP} mode for flights taken in coupled environments shown in Figure 6

543   (RF12 and RF13, both of which primarily sampled single-layer clouds as seen in Figure 1). To

544   examine the effect of coupling on the distribution of N_{CDP}, results for single-layer cases restricted

545   to decoupled environments are separately shown by the dashed line. When comparing the solid

546 and dashed black lines for the properties in all panels, N_{CDP} is the only property shown that

547 significantly diverges for the coupled and decoupled environments. N_{CDP} distributions in single-

548 layer decoupled environments are more similar to distributions of multi-layer clouds than to

549 single-layer cloud distributions in coupled environments. In contrast, the modes for M_{CDP}, σ_{CDP}

550 and MVD_{CDP} are relatively similar in coupled and decoupled environments (all of which are

551 between 0.1–0.3 g m^{-3}, 3–4 μm and ~16 μm, respectively).

552 When comparing single-to multi-layer cases, single-layer cases are slightly skewed to larger

553 M_{CDP} values, whereas both σ_{CDP} and MVD_{CDP} (Figure 7C&D) are skewed to larger values for

554 multi-layer cases. These results suggest multi-layer clouds observed during SOCRATES had less

555 liquid water content than single-layer cases, but broader droplet distributions and larger mean

556 particle sizes. The significance of these differences is tested using Mann-Whitney U-Tests and

557 Kolmogorov-Smirnoff tests. Mann-Whitney U-test determines whether the median of one

558 distribution is significantly greater or less than the other, whereas the two-sample Kolmogorov-

559 Smirnov test determines the significance of the maximum absolute difference between the two

560 cumulative frequency distributions, both of which use lookup tables. These tests do not require

561 prior knowledge of the distributions' shapes. Every test comparing single-layer and the varying

562 multi-layer types' M_{CDP}, σ_{CDP} and MVD_{CDP} rejects the null hypothesis that both sample sets are

563 taken from the same population at a significance level of 10%. These tests were similarly

564 performed for only liquid phase samples to test whether differences are related to the relative

565 phase distributions of liquid and mixed phase samples. For example, available liquid in mixed

566 phase samples may be partitioned to large ice particles which often exceed sizes detectable by

567 the CDP (directly impacting M_{CDP}). However, with the exception of σ_{CDP} in Multi-1st, all the

568   tests reject the null hypothesis, signifying differences in M_{CDP}, σ_{CDP} and MVD_{CDP} for the

569   different cloud types are not related to cloud phase.

570   Parameters in Figure 7 are also separately evaluated within and above the boundary layer for

571   single- and multi-layered clouds in Figure 8 to determine if significant differences exist. Note the

572   relatively low sample size of single-layer samples above the boundary layer might contribute to

573   the multi-modal distributions for N_{CDP} and MVD_{CDP}, although uncertainties associated with the

574   interpolated boundary layer height may be significant as well. Distributions of N_{CDP} and M_{CDP}

575   are shifted towards larger values for multi-layered clouds within the boundary layer, consistent

576   with higher N_{CCN} within the boundary layer. Although distributions of σ_{CDP} and MVD_{CDP} appear

577   similar for both multi-layer cloud cases, Mann-Whitney U-tests and Kolmogorov-Smirnov tests

578   reject the null hypothesis that both sample sets are taken from the same population at a

579   significance level of 10%. Overall, distributions of σ_{CDP} and MVD_{CDP} are more positively

580   skewed for both multi-layer cases compared with the single layer cases, confirming differences

581   in the different cloud types is unrelated to differences in boundary layer and free tropospheric

582   conditions.

583   It is crucial to examine how the properties vary in relation to their location within the cloud layer

584   to get insight into physical processes occurring in the clouds and impacts on vertical profiles of

585   radiative heating. Figure 9 shows joint histograms of both shortwave (solar) and longwave

586   (terrestrial) irradiance as a function of the normalized height within a cloud layer, defined

587   following McFarquhar et al. (2007) as

588
$$1) \quad z_n = \frac{(z - z_{Cloud\_base})}{(z_{Cloud\_top} - z_{Cloud\_base})},$$

26

589   where z refers to the altitude of the local 1 Hz sample, z_{Cloud_top} and z_{Cloud_base} refer to the altitudes

590   of cloud top and cloud base for a particular layer, respectively (i.e., the highest and lowest

591   samples within a layer having $M_{CDP} > 0.01$ g m^{-3}). Cloud layers are split into two categories:

592   those that are the highest layer of their respective regime (top cloud layers; Figure 9A–C) and

593   those that are underlying another cloud layer (non-top cloud layers; Figure 9D–F). Layers in the

594   non-top category are only associated with multi-layer clouds and should receive less solar

595   radiation than top layers. This is precisely what is observed when comparing the solar irradiance

596   (F_{solar}) in Figure 9A&D: most measurements in the top cloud-layers occur between 400 and 600

597   W m^{-2} at $z_n > 0.9$ whereas there are nearly zero ($< \sim 10$) cases of solar irradiance greater than 400

598   W m^{-2} for the non-top cloud layer. Likewise, most measurements of net longwave irradiance

599   (F_{terr_net}) ranges from -110–0 W m^{-2} for the top cloud layer at $z_n > 0.9$, with a mean value of -50

600   W m^{-2}. In contrast, there are nearly zero cases of $F_{terr\_net} < -50$ W m^{-2} for non-top cloud layers.

601   The heating profiles shown in Figure 9C&F reveal relatively weak cloud top cooling associated

602   with longwave radiation for both the top and lower layers. The terrestrial heating rate is

603   computed as

604
$$2) \quad \frac{\partial T}{\partial t} = -\frac{1}{\sum_{i=1}^{3} \rho_i C_{p,i}} \frac{dF_{terr\_net}}{dz}$$

605   where T is temperature, t is time, z is vertical distance, ρ_i is the total density of the air, liquid or

606   ice mass, and $C_{p,i}$ is the specific heat of either air, water or ice at constant pressure (Braslau &

607   Dave, 1975; Petty, 2006). In mixed phase samples, the specific heat of water at constant pressure

608   is used for the entire cloud mass since efforts are not made to derive the cloud mass separately

609   for the ice or liquid phase (therefore there are only two iterations in the summation). However,

610   exchanging it for the specific heat of ice at constant pressure is inconsequential to the results as

611   the air density is significantly greater than that of the cloud mass. Average cooling rates are ~0.5

612   K hr^{-1} for $z_n > 0.9$ for non-top cloud layers, and lower than ~2.5 K hr^{-1} for top cloud layers. Such

613   low cooling rates are associated with emitted longwave radiation from overlying cloud layers for

614   non-top cloud layers, as well as relatively low mass contents of clouds over this region, as seen

615   with M_{CDP} having modes ranging from 0.1–0.2 g m^{-3} for all cloud layer types (Figure 7B).

616   Weaker cooling rates may result in weaker cloud top turbulent mixing for non-top cloud layers,

617   resulting in different lifetimes or evolutions for different cloud layer regimes. Higher cooling

618   rates are associated with greater average liquid mass of the top cloud layers. Specifically,

619   average cloud top cooling rates are 1.5 K hr^{-1} greater for cloud layers with average M_{CDP} above

620   the 50th percentile (0.2 g m^{-3}) than below the 50th percentile (not shown).

621   The clustering of droplets, which can have implications for many factors such as precipitation

622   onset (Raymond A. Shaw et al., 1998) and the evolution of raindrop size distributions

623   (McFarquhar, 2004), is evaluated using joint histograms in Figure 10A,B and Figure 10C,D for

624   all non-top cloud layers and all top cloud layers, respectively. Unlike Figure 9, results are

625   normalized over the respective z_n bins. The clustering index (CI) is a commonly used metric

626   (e.g., Baker, 1992; Chaumat & Brenguier, 2001; Jaczewski & Malinowski, 2005) that is defined

627   as

628    $$3) \quad CI = \left(\frac{V}{M} - 1\right),$$

629   where M is the mean and V the variance of a given parameter over a given number of samples.

630   This metric takes advantage of the fact that a Poisson distribution has an equal mean and

631   variance. By subtracting 1 from V/M, a droplet distribution sampled from a population with a

632   constant mean rate results in CI equaling 0 cm^{-3} (in the case of drop concentrations per cubic

633   centimeter), and CI increases with increasing droplet heterogeneity. Note that CI less than 0 cm^{-3}

634   (V<M) is simply characterized as underdispersed (i.e., having a variance lower than that

635   expected for a Poisson distribution). In this study, CI is calculated every second using 10 Hz

636   observations, providing a measure of inhomogeneity over scales of ~120 m (depending on flight

637   speed). In order to scale results on a logarithmic scale, the subtraction of 1 is removed from Eq.

638   (2) so all results have a minimum possible value greater than 0 cm^{-3}. The altered calculation (i.e.,

639   altered clustering index; ACI) used in this study is given by

640    $$4) \qquad ACI = \log_{10}\left(\frac{V}{M}\right).$$

641   Figure 10A and 10C show ACI for N_{CDP} (ACI_{N_CDP}), whereas figure 10B and 10D show ACI for

642   M_{CDP} (ACI_{M_CDP}). Joint histograms of ACI_{N_CDP} are relatively similar for layers from $0 < z_n <$

643   0.8, with most values between -0.4 and 0.2 cm^{-3}. Near cloud base ($z_n = 0$), ACI_{N_CDP} varies from

644   ~0 to 1 cm^{-3} and average values are slightly greater than those from $0.2 < z_n < 0.8$. Values

645   increase near cloud top, with most ACI_{N_CDP} between 0.5–2 cm^{-3}. Increased droplet clustering

646   has previously been found to occur at cloud top, which has been attributed to mixing and cloud

647   top entrainment in the past (Baker, 1992; Dodson & Small Griswold, 2019; Small & Chuang,

648   2008).

649   Discernable differences in clustering at cloud top are observed between the top and non-top

650   layers near cloud top, which are likely due to differences in entrainment and/or mixing strength.

651   Namely, average ACI_{N_CDP} and ACI_{M_CDP} are greater at cloud top for the top cloud layers

652   compared with non-top layers. The most notable differences are observed for ACI_{M_CDP}, where

653   normalized occurrence frequencies greater than 0.1 exceed ACI_{M_CDP} equal to -1 g m^{-3} only for

654   the top cloud layers. In addition, the variability of ACI_{M_CDP} between cloud top and the

655   underlying cloud is greater for top cloud layers than for non-top layers. These indicators of

656   greater entrainment and/or mixing (e.g., greater clustering values) are expected with greater

657   cooling rates at the top of top cloud layers compared with non-top cloud layers (Figure 9C,F).

658   Other factors may account for the small-scale variability of N_{CDP} and M_{CDP} at cloud top, such as

659   previously observed generating cells (Wang et al., 2020) or upsidence waves (i.e., gravity waves

660   visible within a cloud deck) (Rahn & Garreaud, 2010). The influence of large-scale factors on

661   ACI_{N_CDP} is evaluated in Figure 11, which shows level leg cloud-top observations from two

662   research flights. Satellite imagery for both cases reveal undulations in cloud cover surrounding

663   the two transect regions, although cirrus immediately overly the flight path for RF13 (not

664   shown). The Brunt-Vaisala frequency for both cases is determined (using ambient virtual

665   potential temperature) from nearby sawtooths and is 0.016 rad s^{-1} and 0.027 rad s^{-1} for RF06 and

666   RF13, respectively. These values suggest both environments are conducive for upsidence waves,

667   and are consistent with the lengths of the wavelike structures observed for N_{CDP}. Namely, that

668   the wavelength is longer for RF06 (~15 km; Figure 11A) than for RF13 (~2 km; Figure 11B).

669   Autocorrelations of N_{CDP} for RF06 (Figure 11C) and RF13 (Figure 11D) capture the wavelike

670   structures of N_{CDP}, having peak autocorrelation values above the bands of rejection at lags of 15

671   km for RF06 and at ~2 km, 4.5 km and 7 km for RF13. Jiang & Wang (2012) found evidence

672   that liquid water content increases in the regions of upward motion from upsidence waves. A

673   similar analysis is performed for both cases using M_{CDP} and a similar wavelike structure and

674   autocorrelation is found for RF06, although not for RF13 (not shown).

675   For both cases, ACI_{N_CDP} does not possess the wavelike structures observed for N_{CDP}, which is

676   observed when applying autocorrelations to ACI_{N_CDP}. A wavelike structure in ACI_{N_CDP} appears

677   in RF06, but most amplitudes do not exceed the significance bounds. In contrast,

678   autocorrelations exceed the significance bounds for N_{CDP} at lags comparable to the observed

679   wavelengths (e.g., a 15 km wavelength where peak N_{CDP} are observed at ~5±2 km and 20±3 km

680   for RF06). Correlations of N_{CDP} and ACI_{N_CDP} are -0.10 and -0.46 for RF06 and RF13,

681   respectively. Increases in ACI_{N_CDP} often correspond with decreases in N_{CDP} (e.g., at 2.5 km and

682   12 km for RF13, Figure 11B), consistent with trends expected from entrainment-mixing.

683   Average normalized cloud particle size distributions, such that the integrated concentration

684   equals one, are shown in Figure 12. Specifically, normalized size distributions are obtained by

685   weighting number concentrations of the respective bins by the total cloud particle concentration.

686   Distributions include contributions from both the CDP and 2DS and are normalized over their

687   combined range (2–1280 μm). To characterize their height variation, normalized particle size

688   distributions are first interpolated to a 2D grid with z_n spaced over 0.01 intervals. Additionally,

689   normalized particle size distributions are interpolated to the 2D grid over 80 logarithmically

690   scaled bins ranging from 2–1280 μm. Results are then smoothed using a two-dimensional

691   convolution and a 3x3 box kernel (i.e., averaging kernel). This method is analogous to that

692   commonly used in image smoothing (Kim & Casper, 2013), allowing for a clear visual depiction

693   of particle size distributions over the range of z_n. Focusing on the top cloud layers (Figure 12A),

694   the maximum normalized $N(\log(D))$ (i.e., $dN/d\log(D)$) > 0.01 at $z_n < 0.1$ occurs at D from 2 to

695   20 μm. These maximum $N(\log(D))$ shift towards larger sizes with increasing z_n. At $z_n > 0.6$,

696   maximum normalized $N(\log(D)) > 0.05)$ occur at D from approximately 10 to 30 μm. This shift

697   is consistent with droplet activation occurring near cloud base producing small droplets, which

698   grow with increasing height due to condensational growth and collision-coalescence.

699   There are notable differences for the non-top cloud layers (Figure 12D) compared to the top

700   cloud layers (Figure 12A). The non-top layers have greater small droplet concentrations at $z_n >$

701   0.4 compared to the top layers with normalized $N(\log(D))$ at $D < 10$ µm being ~0.05 throughout

702   the entire cloud depth, whereas values at $D < 10$ µm decrease well below 0.01 for $z_n > 0.5$ in top

703   cloud layers (green shading). Further, $N(\log(D))$ greater than 0.01 reach sizes up to 40 µm

704   throughout most of the cloud for non-top cloud layers. This is not seen for the top cloud layers

705   throughout most of the cloud. These trends highlight the differences seen in Figure 7C&D,

706   namely that non-top cloud layers which only occur in multi-layer clouds have broader droplet

707   size distributions. These broader distributions contain larger relative frequencies of both smaller

708   ($D < 10$ µm) and larger (D from 30–50 µm) drops. Purple lines show the average σ of D for the

709   normalized size distributions, and these values are larger for non-top cloud layers compared to

710   top cloud layers over the entire depth. Normalized $N(\log(D))$ at $D > 50$ µm are also greater for

711   the non-top cloud layers throughout the cloud depth.

712   Broader distributions are likely related to a greater frequency of mixed phase samples within

713   non-top cloud layers, which may be associated with a broader range of ice crystals. This is

714   suggested by plotting results separately for liquid phase samples (Figure 12B,E) and mixed phase

715   samples (Figure 12C,F); normalized values of $D > 10^2$ µm are clearly greater for the mixed phase

716   samples of both top- and non-top cloud layers compared with liquid phase samples. However,

717   differences in cloud phase frequency do not account for all the observed differences between the

718   layer types. Non-top cloud layers still have broader drop size distributions ($D < 50$ µm) than top

719   cloud layers regardless of the cloud phase, which is likely due to particle interactions occurring

720   vertically through local cloud layers. This is confirmed by computing average σ_{CDP} within the

721   vertical profile, which shows values are ~0.5 µm greater for liquid phase samples and ~1.5 µm

722   greater for mixed phase samples in non-top cloud layers at $z_n > 0.5$ (not shown). In fact, average

723   ice concentrations in mixed phase samples with maximum dimensions exceed 200 µm

724   (aspherical $N_{2DS\_D>200\mu m}$) are nearly an order of magnitude greater in non-top cloud layers (1.7 L^{-}

725   ^{1}) than top layers (0.2 L^{-1}). The average σ are much lower for mixed phase samples in the top

726   cloud layers compared with non-top layers. This is due to mixed phase samples in the top cloud

727   layers having much greater drop concentrations (average N_{CDP} = 120 cm^{-3}) than non-top cloud

728   layers (average N_{CDP} = 40 cm^{-3}). Similarly, drop concentrations are greater in the top layers for

729   liquid phase samples as well (average N_{CDP} = 110 cm^{-3}) than non-top layers (average N_{CDP} = 70

730   cm^{-3}), consistent with the lowest N_{CDP} observed for the lowest cloud layers in Figure 7A. The

731   higher concentrations in top cloud layers are observed even when removing samples from

732   coupled environments, which causes the average N_{CDP} of top layers to decrease ~10 cm^{-3} for both

733   phases.

734   3.4 Vertical distributions of phase and average cloud properties

735   In addition to characterizing multi-layer clouds based on the relative height within the cloud

736   layer and based on whether in the top or non-top cloud layer, the relative frequency of liquid

737   phase with respect to z_n is shown in Figure 13. Results for multi-layer clouds are sorted by cloud

738   height relative to the lowest cloud layer (as in Figure 2&7; left panel) or by the lowest, middle

739   and highest layers (right panel). Results for the lowest cloud layers (Multi-1st and Multi-lowest)

740   are the same for both categorizations. Single-layer clouds are seen to contain the most liquid

741   phase samples, which is consistent with Figure 2B. Furthermore, the liquid phase frequency is

742   lowest for $z_n < 0.4$, which is similar to previous findings that Arctic single-layer mixed phase

743   clouds contain the highest frequency of ice particles in the lower half of the cloud (McFarquhar

744   et al., 2007; Mioche et al., 2017). The lowest cloud layers in multi-layer clouds have much lower

745   liquid phase frequencies than in single-layer cases (consistent with Figure 2B), with liquid phase

746   frequencies decreasing from 0.75 to 0.60 from cloud base to cloud top.

747   For multi-layer clouds, the second and third highest layers (Multi-2nd and Multi-3rd,

748   respectively; Figure 13A) have liquid frequencies varying between 0.75 to 0.95 throughout the

749   normalized heights. Cloud layers overlying the third highest layers have lower liquid phase

750   frequencies which are comparable to the lowest cloud layers, varying from 0.55 to 0.70

751   throughout their depth. These layers typically occur at lower temperatures. Figure 13B shows

752   results discriminating multi-layer clouds into the highest (Multi-top) and layers residing between

753   the highest and lowest cloud layers (Multi-middle). The middle layers have much lower liquid

754   phase frequencies compared with the top cloud layers. In fact, the liquid phase frequencies are

755   comparable between the middle and lowest layers, whereas the highest cloud layers have liquid

756   phase frequencies comparable to single-layers. Note that Multi-grt3 has frequencies resembling

757   middle layers rather than the top layers, because top layers are heavily weighted by cases where

758   there are only two cloud layers in the atmospheric column. The phase frequency structure of

759   multi-layer clouds is consistent with what would be expected from a prominent seeder-feeder

760   mechanism. Primary nucleation may occur at the highest cloud layers where temperatures are

761   lowest, of which 61% were between -10° and 0°C and 78% between -20° to 0°C. Low liquid

762   frequencies at the top of the lowest cloud layers may indicate seeding from above.

763   The remainder of the findings address how other microphysical properties vary as a function of

764   z_n for the different layers, whose sample sizes are found in Figure 13. Figure 14 shows vertical

765   profiles for single-layer clouds. Results are separately shown for liquid and mixed phase samples

766   by the red and green lines, respectively. Ice phase samples are not included due to the relatively

767   small sample size of ice phase compared with mixed phase samples (e.g., blue text in Figure 2B).

768   The top row shows N_{CDP}, M_{CDP} and number weighted mean diameter reported by the CDP

769   (Mean D_{CDP}) (Figure 14A–C). All of these variables, with the exception of N_{CDP} for mixed phase

770   samples, increase with height. The discussion for the remainder of this section focuses on liquid

771   phase samples due to (1) the small sample size of mixed phase observations for all cloud layers

772   and (2) the fact that such observations do not necessarily represent a secondary vertical structure,

773   because the majority of mixed phase samples were embedded within primarily liquid phase

774   cloud layers.

775   Figure 14E-G shows vertical profiles for the properties of particles with dimensions greater than

776   50 μm (N_{2DS}, M_{2DS} and Mean D_{2DS}). Both N_{2DS} and M_{2DS} increase with z_n, whereas Mean D_{2DS}

777   decreases with z_n. Note that M_{2DS} and Mean D_{2DS} are larger for mixed phase throughout most of

778   the cloud depth, consistent with the coexistence of larger particles which are primarily ice.

779   Mixed phase Mean D_{2DS} were separately determined for spherical and non-spherical particles

780   greater than 200 μm, and Mean D_{2DS} for non-spherical particles were greater than spherical

781   particles at all z_n (not shown). Figure 14H shows ACI_{N_CDP}, which has a U-shaped distribution

782   similar to Figure 10A&C meaning that maximum ACI_{N_CDP} are at cloud base and cloud top.

783   Vertical profiles of RH in Figure 14D are ~100% throughout the cloud depth, with a deviation of

784   ~95% at cloud top. Black dots with dashed lines show RH for clear-sky regions which primarily

785   occur above cloud top ($z_n > 1.0$). Since the layer classification allows for clear-sky samples to

786   exist within a profile, such samples (although very few) may also occur within a cloud layer ($0 <$

787    $z_n < 1$). The analysis of RH is also shown above cloud top and below cloud base ($z_n > 1$ and $z_n <$

788   0, respectively). Above cloud top and below cloud base data is simply the neighboring 1 Hz

789   clear-sky samples to the respective cloud edges. Clear-sky samples below cloud base are nearly

790   saturated, whereas clear-sky samples above cloud top have an average RH of 60%, with

791   significant variability (standard deviation of ~25%).

792   Figure 15 shows vertical profiles for the lowest cloud layer in multi-layer clouds. Similar to

793   single-layers, M_{CDP}, Mean D_{CDP}, and N_{2DS} all increase with height. Average ACI_{N_CDP} and Mean

794   D_{2DS} have similar distributions, with peak values near cloud top and cloud base for ACI_{N_CDP} and

795   decreasing values with height for Mean D_{2DS}. Differences between the cloud layer types are

796   primarily observed for N_{CDP} and RH, where N_{CDP} roughly decreases with height and clear-sky

797   RH above cloud top is nearly saturated (~96%) with little variance (standard deviation~3%) for

798   the lowest layer in the multi-layer clouds.

799   Figure 16 shows a similar analysis for the top cloud layers (Figure 16A–D), the non-top cloud

800   layers (Figure 16E–H), and middle layers (Figure 16I–L) of multi-layer clouds. Average N_{CDP},

801   Mean D_{CDP}, N_{2DS} and RH are shown for the layer types. N_{CDP} increases with increasing height

802   and peaks above z_n=0.5 for top cloud layers, and below 0.5 for non-top layers. When removing

803   single-layer clouds from the top cloud layer analysis, N_{CDP} similarly peaks above z_n=0.5

804   (supplementary Figure A). Mean D_{CDP} increases with height for all layer types. However,

805   differences are observed in the overlying clear-sky RH for the top and non-top layers. Similar to

806   the differences in single- and lowest multi-layer clouds (Figure 14D,15D), the air is nearly

807   saturated above non-top cloud layers while RH is only ~70% above top layers. When separately

808   evaluating highest multi-layer clouds and removing single-layer clouds from the analysis, the

809   overlying RH is ~90% (supplementary Figure B). Differences in overlying RH may be expected

810   as single-layer clouds will often be capped by rather strong inversions, whereas layers above one

811   another will be associated with weaker inversions. In contrast, reduced longwave cooling at

812   cloud top will be associated with underlying cloud layers of multi-layer regimes rather than top

813   cloud layers.

814

815   4: Discussion

816   The results presented in Section 3 showed the dependence of cloud phase on relative cloud layer

817   height, and on INP and CCN concentrations. There is a clear tendency for underlying cloud

818   layers of multi-layer clouds to have greater frequencies of ice-containing samples, regardless of

819   whether cloud layers were classified by the height relative to the lowest cloud layer or by

820   bottom, middle and highest layers. The frequency of precipitating ice in-between cloud layers

821   was examined to test whether its presence was associated with a prominent seeder-feeder

822   mechanism. About 70% of precipitating samples in-between cloud layers contain ice (Figure

823   3D), and the large frequency of precipitating samples as well as nearly saturated samples within

824   cloud layers (Figure 3C) is further evidence of a prominent seeder-feeder mechanism over the

825   region.

826   The distribution and vertical structure of drop clustering was characterized to compare against

827   previous studies that examined entrainment-mixing and its impacts based on drop size

828   distribution inhomogeneities (Bower & Choularton, 1988; Paluch, 1986; Paluch & Knight,

829   1984). Entrainment-mixing is often characterized as homogeneous or inhomogeneous.

830   Homogeneous mixing characteristically results in a shift of drop size distributions towards

831   smaller drop sizes due to rapid mixing causing all droplets to experience partial evaporation,

832   whereas inhomogeneous mixing results in a reduction of droplet number concentrations but not

833   in droplet sizes due to slower mixing causing different drops to experience different amounts of

834   subsaturation (Baker et al., 1980; Latham & Reed, 1977). The latter pertains to *extreme*

835   inhomogeneous mixing, whereas most mixing events do not necessarily follow one or the other

836   extreme (e.g., Korolev et al., 2016).

837   Drop clustering was greater at cloud top of the highest cloud layers (including single layer

838   clouds) compared with underlying layers, likely due to differences in entrainment and mixing

839   strength between the different layer types. Lower clustering values at cloud top, as well as the

840   lower variability of these values between cloud top ($z_n > 0.9$) and the cloud beneath ($z_n < 0.9$) for

841   the underlying layers compared with the highest cloud layers (Figure 10), is consistent with

842   weaker entrainment-mixing (potentially indicative of extreme inhomogeneous mixing) for

843   underlying layers. It is important to note that clustering values are sensitive to the spatial scales

844   used (e.g., Baker & Lawson, 2010) and can be computed in different ways, such as utilizing drop

845   interarrival times to determine clustering values on smaller scales, of which further information

846   can be found in Kostinski & Shaw (2001) and Shaw et al. (2002). The purpose of this study is to

847   compare relative differences between cloud layer types, rather than provide an absolute measure

848   of clustering. Clustering on the order of tens to a hundred meters (used here) has previously been

849   directly correlated with entrainment and associated mixing (e.g., Dodson & Small Griswold,

850   2019; Small & Chuang, 2008).

851   The mixing of nearly saturated air would have a diminished impact on drop populations

852   compared with considerably subsaturated air. Namely, the mixing of drier air likely results in

853   local pockets of evaporation on relatively large spatial-scales, which increases drop clustering

854   (e.g., Baker, 1992). The drier air above-cloud for top layers compared with non-top layers

855   (Figure 16D,H) is consistent with greater cloud top clustering for the top layers. The saturated air

856   overlying non-top cloud layers may be important, as previous modeling studies have shown the

857   presence of humidity inversions are required to maintain low-level mixed phase clouds in the

858   Arctic (Curry, 1986; Curry et al., 1988; Solomon et al., 2011). The saturated air could also be

859   associated with evaporating drizzle or sublimating ice from overlying cloud layers. Following

860 Pruppacher & Klett, (1996) and Lamb & Verlinde (2011), a spherical ice particle ranging from

861 D=50 to 150 um in environments having RH with respect to ice ranging from 60% to 80% at

862 temperatures ranging from -20° to 0°C results in ice particles which can fall for distances ranging

863 tens of meters to ~1.5 km before completely sublimating. In this study, cloud top observations

864 less than 200 m from the overlying cloud layer account for 47% of the cases, and observations

865 less than 1 km from the overlying cloud account for 86%, showing that seeding would be

866 expected to have an impact.

867 Despite differences in above cloud RH as well as cloud top clustering and cooling rates for top

868 and non-top layers, droplets greater than 50 μm are observed at cloud top of all layer types with

869 average concentrations ranging from ~20–50 L^{-1} (Figure 16C,G). Other factors may contribute to

870 the common occurrence of droplet diameters exceeding 50 μm, such as sea salt acting as giant

871 CCN (e.g., CCN with maximum dimensions exceeding 2 μm; Jensen & Nugent, (2017)).

872 Additionally, mean D_{2DS} generally increases from cloud top towards cloud base (Figure

873 14G,15G), suggesting collision-coalescence may begin near cloud top.

874 4: Conclusions

875 The microphysical properties of single- and multi-layer clouds over the Southern Ocean were

876 evaluated and contrasted using airborne in situ observations acquired during SOCRATES. Cloud

877 layers were classified using a novel smoothing method applied to in-situ cloud observations

878 acquired during sawtooths of the aircraft. This resulted in 55 profiles of single-layer clouds and

879 183 profiles of individual multi-layer clouds. Single-layer clouds have greater cloud liquid

880 droplet mass and number concentrations than multi-layer clouds, with number concentrations in

881 single-layer clouds from two research flights in coupled environments approximately double

882 those in decoupled environments. Multi-layer clouds have broader drop size distributions than

883 single-layer clouds. When cloud layers are separated according to whether they are underlying

884 other cloud layers (non-top cloud layers) or not (top cloud layers), non-top cloud layers have

885 broader drop size distributions (D<50 μm) and total particle size distributions throughout the

886 vertical cloud depth compared to top cloud layers.

887 The liquid phase most frequently occurs in single-layer clouds compared with multi-layer clouds.

888 Liquid phase frequencies in multi-layer clouds are the lowest in the lowest cloud layers and

889 increase with higher cloud layers until the third highest layer is reached, suggesting a prominent

890 seeder-feeder presence in multi-layer clouds (Figure 2B). When classifying the layers of multi-

891 layer clouds as lowest, highest, and those lying in-between, the highest cloud layers have the

892 greatest frequency of liquid phase samples, and the middle layers have similarly low relative

893 frequencies as the lowest layers (Figure 13B). These findings show that caution should be taken

894 when quantifying cloud phase frequencies solely from satellite imagery due to potential biases in

895 cloud top phase as well as overlapping cloud layers, as well as caution in classifying phase

896 frequency by temperature alone.

897 Relative phase frequencies are also explored in relation to CCN and INP concentrations. There is

898 some evidence of INP concentrations being positively related to ice frequencies (e.g., a

899 correlation of -0.41 is observed for INP with activation temperatures from -30° to -10°C and

900 liquid phase frequencies from -20° to -2°C in the boundary layer), but it is only observed for

901 select temperature and INP activation temperature ranges (Figure 4). The lack of a relation for

902 other temperature and activation temperatures suggests alternative processes, such as secondary

903 ice production and accretion, play a major role in phase determination. Phase frequencies are

904 found to be directly related to CCN concentrations, but only above the boundary layer and

905   primarily at temperatures less than -10°C (Figure 5). Namely, ice is less likely to be observed in

906   such environments with high CCN concentrations.

907   The dependence of cloud microphysical properties on cloud layer normalized height was also

908   examined. The number weighted mean diameter of drops less than 50 μm increases with height

909   for all cloud layer types, whereas number concentrations peak near cloud top for top cloud layers

910   and near cloud base for non-top cloud layers (Figure 12). The number concentration and mass of

911   drops greater than 50 μm also increase with cloud height, whereas the mean diameter decreases

912   with increasing height. These similarities are observed between single- and multi-layer clouds in

913   spite of differences in cloud top droplet clustering, radiative cooling profiles, overlying RH and

914   relative phase frequencies, highlighting a propensity for precipitation initiation in both single and

915   multi-layer clouds. However, robust differences in the microphysical properties of single- and

916   multi-layer clouds warrants further investigation to distinguish and constrain physical responses

917   resulting in the differences provide here.

41

937

938 Bibliography

939 Ahn, E., Huang, Y., Chubb, T. H., Baumgardner, D., Isaac, P., de Hoog, M., et al. (2017). In situ
940 observations of wintertime low-altitude clouds over the Southern Ocean. *Quarterly Journal of*
941 *the Royal Meteorological Society*, *143*(704), 1381–1394. https://doi.org/10.1002/qj.3011

942 Ahn, E., Huang, Y., Siems, S. T., & Manton, M. J. (2018). A Comparison of Cloud
943 Microphysical Properties Derived From MODIS and CALIPSO With In Situ Measurements
944 Over the Wintertime Southern Ocean. *Journal of Geophysical Research: Atmospheres*, *123*(19),
945 11,120-11,140. https://doi.org/10.1029/2018JD028535

946 Alexander, S. P., McFarquhar, G. M., Marchand, R., Protat, A., Vignon, É., Mace, G. G., &
947 Klekociuk, A. R. (2021). Mixed-Phase Clouds and Precipitation in Southern Ocean Cyclones and
948 Cloud Systems Observed Poleward of 64°S by Ship-Based Cloud Radar and Lidar. *Journal of*
949 *Geophysical Research: Atmospheres*, *126*(8), e2020JD033626.
950 https://doi.org/10.1029/2020JD033626

951 Atlas, R. L., Bretherton, C. S., Blossey, P. N., Gettelman, A., Bardeen, C., Lin, P., & Ming, Y.
952 (2020). How Well Do Large-Eddy Simulations and Global Climate Models Represent Observed
953 Boundary Layer Structures and Low Clouds Over the Summertime Southern Ocean? *Journal of*
954 *Advances in Modeling Earth Systems*, *12*(11), e2020MS002205.
955 https://doi.org/10.1029/2020MS002205

956   Baker, B., & Lawson, R. P. (2010). Analysis of tools used to quantify droplet clustering in
957   clouds. *Journal of the Atmospheric Sciences*, *67*(10), 3355–3367.
958   https://doi.org/10.1175/2010JAS3409.1

959   Baker, B. A. (1992). Turbulent entrainment and mixing in clouds: a new observational approach.
960   *Journal of the Atmospheric Sciences*, *49*(5), 387–404. https://doi.org/10.1175/1520-
961   0469(1992)049<0387:TEAMIC>2.0.CO;2

962   Baker, M. B., Corbin, R. G., & Latham, J. (1980). The influence of entrainment on the evolution
963   of cloud droplet spectra: I. A model of inhomogeneous mixing. *Quarterly Journal of the Royal*
964   *Meteorological Society*, *106*(449), 581–598. https://doi.org/10.1002/qj.49710644914

965   Baumgardner, D., & Korolev, A. (1997). Airspeed corrections for optical array probe sample
966   volumes. *Journal of Atmospheric and Oceanic Technology*, *14*(5), 1224–1229.
967   https://doi.org/10.1175/1520-0426(1997)014<1224:ACFOAP>2.0.CO;2

968   Bodas-Salcedo, A., Hill, P. G., Furtado, K., Williams, K. D., Field, P. R., Manners, J. C., et al.
969   (2016). Large Contribution of Supercooled Liquid Clouds to the Solar Radiation Budget of the
970   Southern Ocean. *Journal of Climate*, *29*(11), 4213–4228. https://doi.org/10.1175/JCLI-D-15-
971   0564.1

972   Boers, R., Jensen, J. B., Krummel, P. B., & Gerber, H. (1996). Microphysical and short-wave
973   radiative structure of wintertime stratocumulus clouds over the Southern Ocean. *Quarterly*
974   *Journal of the Royal Meteorological Society*, *122*(534), 1307–1339.
975   https://doi.org/10.1002/qj.49712253405

976   Boers, R., Jensen, J. B., & Krummel, P. B. (1998). Microphysical and short-wave radiative
977   structure of stratocumulus clouds over the Southern Ocean: Summer results and seasonal
978   differences. *Quarterly Journal of the Royal Meteorological Society*, *124*(545), 151–168.
979   https://doi.org/10.1002/qj.49712454507

980   Bower, K. N., & Choularton, T. W. (1988). The effects of entrainment on the growth of droplets
981   in continental cumulus clouds. *Quarterly Journal of the Royal Meteorological Society*, *114*(484),
982   1411–1434. https://doi.org/10.1002/qj.49711448404

983   Braslau, N., & Dave, J. V. (1975). Atmospheric Heating Rates Due to Solar Radiation for
984   Several Aerosol-Laden Cloudy and Cloud-Free Models. *Journal of Applied Meteorology (1962-*
985   *1982)*, *14*(3), 396–399.

986   Chaumat, L., & Brenguier, J. L. (2001). Droplet spectra broadening in cumulus clouds. Part II:
987   Microscale droplet concentration heterogeneities. *Journal of the Atmospheric Sciences*, *58*(6),
988   642–654. https://doi.org/10.1175/1520-0469(2001)058<0642:DSBICC>2.0.CO;2

989   Christensen, M. W., Carrió, G. G., Stephens, G. L., & Cotton, W. R. (2013). Radiative impacts
990   of free-tropospheric clouds on the properties of marine stratocumulus. *Journal of the*
991   *Atmospheric Sciences*, *70*(10), 3102–3118. https://doi.org/10.1175/JAS-D-12-0287.1

Chubb, T., Huang, Y., Jensen, J., Campos, T., Siems, S., & Manton, M. (2016). Observations of high droplet number concentrations in Southern Ocean boundary layer clouds. *Atmospheric Chemistry and Physics*, *16*(2), 971–987. https://doi.org/10.5194/acp-16-971-2016

Chubb, T. H., Jensen, J. B., Siems, S. T., & Manton, M. J. (2013). In situ observations of supercooled liquid clouds over the Southern Ocean during the HIAPER Pole-to-Pole Observation campaigns. *Geophysical Research Letters*, *40*(19), 5280–5285. https://doi.org/10.1002/grl.50986

Collins, W. D. (2001). Parameterization of generalized cloud overlap for radiative calculations in general circulation models. *Journal of the Atmospheric Sciences*, *58*(21), 3224–3242. https://doi.org/10.1175/1520-0469(2001)058<3224:POGCOF>2.0.CO;2

Cooper, W. A., Friesen, R. B., Hayman, M., Jensen, J. B., Lenschow, D. H., Romashkin, P. A., et al. (2016). *Characterization of Uncertainty in Measurements of Wind From the NSF/NCAR Gulfstream V Research Aircraft*. Retrieved from https://opensky.ucar.edu/islandora/object/technotes%3A540/datastream/PDF/download/Characterization_of_Uncertainty_in_Measurements_of_Wind_from_the_NSF_NCAR_Gulfstream_V_Research_Aircraft.citation

Coopman, Q., Riedi, J., Zeng, S., & Garrett, T. J. (2020). Space-Based Analysis of the Cloud Thermodynamic Phase Transition for Varying Microphysical and Meteorological Regimes. *Geophysical Research Letters*, *47*(6), e2020GL087122. https://doi.org/10.1029/2020GL087122

Curry, J. A. (1986). Interactions among turbulence, radiation and microphysics in Arctic stratus clouds. *Journal of the Atmospheric Sciences*, *43*(1), 90–106. https://doi.org/10.1175/1520-0469(1986)043<0090:IATRAM>2.0.CO;2

Curry, J. A., Ebert, E. E., & Herman, G. F. (1988). Mean and turbulence structure of the summertime Arctic cloudy boundary layer. *Quarterly Journal of the Royal Meteorological Society*, *114*(481), 715–746. https://doi.org/10.1002/qj.49711448109

D'Alessandro, J. J., Diao, M., Wu, C., Liu, X., Jensen, J. B., & Stephens, B. B. (2019). Cloud phase and relative humidity distributions over the Southern Ocean in austral summer based on in situ observations and CAM5 simulations. *Journal of Climate*, *32*(10), 2781–2805. https://doi.org/10.1175/JCLI-D-18-0232.1

D'Alessandro, J. J., McFarquhar, G. M., Wu, W., Stith, J. L., Jensen, J. B., & Rauber, R. M. (2021). Characterizing the Occurrence and Spatial Heterogeneity of Liquid, Ice, and Mixed Phase Low-Level Clouds Over the Southern Ocean Using in Situ Observations Acquired During SOCRATES. *Journal of Geophysical Research: Atmospheres*, *126*(11), e2020JD034482. https://doi.org/10.1029/2020JD034482

DeMott, P. J., Hill, T. C. J., Petters, M. D., Bertram, A. K., Tobo, Y., Mason, R. H., et al. (2017). Comparative measurements of ambient atmospheric concentrations of ice nucleating particles using multiple immersion freezing methods and a continuous flow diffusion chamber.

Atmospheric Chemistry and Physics, *17*(18), 11227–11245. https://doi.org/10.5194/acp-17-11227-2017

Diao, M. (2021). VCSEL 1 Hz water vapor data: UCAR/NCAR—Earth Observing Laboratory. Retrieved from https://data.eol.ucar.edu/dataset/552.051

Dodson, D. S., & Small Griswold, J. D. (2019). Droplet inhomogeneity in shallow cumuli: The effects of in-cloud location and aerosol number concentration. *Atmospheric Chemistry and Physics*, *19*(11), 7297–7317. https://doi.org/10.5194/acp-19-7297-2019

Eloranta, E. E. (2006). High Spectral Resolution Lidar. In *Lidar* (pp. 143–163). Springer-Verlag. https://doi.org/10.1007/0-387-25101-4_5

Engeln, A. von, & Teixeira, J. (2013). A Planetary Boundary Layer Height Climatology Derived from ECMWF Reanalysis Data. *Journal of Climate*, *26*(17), 6575–6590. https://doi.org/10.1175/JCLI-D-12-00385.1

Fiddes, S. L., Protat, A., Mallet, M. D., Alexander, S. P., & Woodhouse, M. T. (2022). Southern Ocean cloud and shortwave radiation biases in a nudged climate model simulation: does the model ever get it right? Retrieved April 11, 2022, from https://acp.copernicus.org/preprints/acp-2022-259/

Field, P. R., Wood, R., Brown, P. R. A., Kaye, P. H., Hirst, E., Greenaway, R., & Smith, J. A. (2003). Ice particle interarrival times measured with a fast FSSP. *Journal of Atmospheric and Oceanic Technology*, *20*(2), 249–261. https://doi.org/10.1175/1520-0426(2003)020<0249:IPITMW>2.0.CO;2

Field, P. R., Heymsfield, A. J., & Bansemer, A. (2006). Shattering and particle interarrival times measured by optical array probes in ice clouds. *Journal of Atmospheric and Oceanic Technology*, *23*(10), 1357–1371. https://doi.org/10.1175/JTECH1922.1

Filioglou, M., Mielonen, T., Balis, D., Giannakaki, E., Arola, A., Kokkola, H., et al. (2019). Aerosol Effect on the Cloud Phase of Low-Level Clouds Over the Arctic. *Journal of Geophysical Research: Atmospheres*, *124*(14), 7886–7899. https://doi.org/10.1029/2018JD030088

Finlon, J. A., McFarquhar, G. M., Nesbitt, S. W., Rauber, R. M., Morrison, H., Wu, W., & Zhang, P. (2019). A novel approach for characterizing the variability in mass–dimension relationships: results from MC3E. *Atmospheric Chemistry and Physics*, *19*(6), 3621–3643. https://doi.org/10.5194/acp-19-3621-2019

Finlon, J. A., Rauber, R. M., Wu, W., Zaremba, T. J., McFarquhar, G. M., Nesbitt, S. W., et al. (2020). Structure of an Atmospheric River Over Australia and the Southern Ocean: II. Microphysical Evolution. *Journal of Geophysical Research: Atmospheres*, *125*(18). https://doi.org/10.1029/2020JD032514

1064 Fleishauer, R. P., Larson, V. E., & Vonder Haar, T. H. (2002). Observed microphysical structure
1065 of midlevel, mixed-phase clouds. *Journal of the Atmospheric Sciences*, *59*(11), 1779–1804.
1066 https://doi.org/10.1175/1520-0469(2002)059<1779:OMSOMM>2.0.CO;2

1067 Gettelman, A., Bardeen, C. G., McCluskey, C. S., Järvinen, E., Stith, J., Bretherton, C., et al.
1068 (2020). Simulating Observations of Southern Ocean Clouds and Implications for Climate.
1069 *Journal of Geophysical Research: Atmospheres*, *125*(21), e2020JD032619.
1070 https://doi.org/10.1029/2020JD032619

1071 Hallett, J., & Mossop, S. C. (1974). Production of secondary ice particles during the riming
1072 process. *Nature*, *249*(5452), 26–28. https://doi.org/10.1038/249026a0

1073 Hande, L. B., Siems, S. T., Manton, M. J., & Belusic, D. (2012). Observations of wind shear
1074 over the Southern Ocean. *Journal of Geophysical Research: Atmospheres*, *117*(D12).
1075 https://doi.org/10.1029/2012JD017488

1076 Haynes, J. M., Jakob, C., Rossow, W. B., Tselioudis, G., & Brown, J. B. (2011). Major
1077 characteristics of Southern Ocean cloud regimes and their effects on the energy budget. *Journal*
1078 *of Climate*, *24*(19), 5061–5080. https://doi.org/10.1175/2011JCLI4052.1

1079 Herman, G., & Goody, R. (1976). Formation and Persistence of Summertime Arctic Stratus
1080 Clouds. *Journal of the Atmospheric Sciences*, *33*(8), 1537–1553. https://doi.org/10.1175/1520-
1081 0469(1976)033<1537:FAPOSA>2.0.CO;2

1082 Heymsfield, A. J., & Parrish, J. L. (1978). Computation Technique for increasing The Effective
1083 Sampling Volume of The PMS Two-Dimensional Particle Size Spectrometer. *Journal of Applied*
1084 *Meteorology*, *17*(10), 1566–1572. https://doi.org/10.1175/1520-
1085 0450(1978)017<1566:ACTFIT>2.0.CO;2

1086 Heymsfield, A. J., Field, P. R., Bailey, M., Rogers, D., Stith, J., Twohy, C., et al. (2011). Ice in
1087 clouds experiment-layer clouds. Part I: Ice growth rates derived from lenticular wave cloud
1088 penetrations. *Journal of the Atmospheric Sciences*, *68*(11), 2628–2654.
1089 https://doi.org/10.1175/JAS-D-11-025.1

1090 Hobbs, P. V., & Rangno, A. L. (1998). Microstructures of low and middle-level clouds over the
1091 Beaufort Sea. *Quarterly Journal of the Royal Meteorological Society*, *124*(550), 2035–2071.
1092 https://doi.org/10.1002/qj.49712455012

1093 Holroyd, E. W. (1987). Some Techniques and Uses of 2D-C Habit Classification Software for
1094 Snow Particles. *Journal of Atmospheric and Oceanic Technology*, *4*(3), 498–511.
1095 https://doi.org/10.1175/1520-0426(1987)004<0498:stauoc>2.0.co;2

1096 Houze, R. A. (2014). Cloud Dynamics - Second Edition. In *International Geophysics* (Vol. 104,
1097 pp. 1–432). Academic Press. https://doi.org/10.1016/B978-0-12-374266-7.00001-9

1098 Hu, Y., Winker, D., Vaughan, M., Lin, B., Omar, A., Trepte, C., et al. (2009).
1099 CALIPSO/CALIOP cloud phase discrimination algorithm. *Journal of Atmospheric and Oceanic*
1100 *Technology*, *26*(11), 2293–2309. https://doi.org/10.1175/2009JTECHA1280.1

1101 Huang, Y., Siems, S. T., Manton, M. J., & Thompson, G. (2014). An Evaluation of WRF
1102 Simulations of Clouds over the Southern Ocean with A-Train Observations. *Monthly Weather*
1103 *Review*, *142*(2), 647–667. https://doi.org/10.1175/MWR-D-13-00128.1

1104 Huang, Y., Franklin, C. N., Siems, S. T., Manton, M. J., Chubb, T., Lock, A., et al. (2015).
1105 Evaluation of boundary-layer cloud forecasts over the Southern Ocean in a limited-area
1106 numerical weather prediction system using in situ , space-borne and ground-based observations.
1107 *Quarterly Journal of the Royal Meteorological Society*, *141*(691), 2259–2276.
1108 https://doi.org/10.1002/qj.2519

1109 Huang, Y., Siems, S. T., & Manton, M. J. (2021). Wintertime In Situ Cloud Microphysical
1110 Properties of Mixed-Phase Clouds Over the Southern Ocean. *Journal of Geophysical Research:*
1111 *Atmospheres*, *126*(11), e2021JD034832. https://doi.org/10.1029/2021JD034832

1112 Hudson, J. G., & Frisbie, P. R. (1991). Cloud condensation nuclei near marine stratus. *Journal of*
1113 *Geophysical Research*, *96*(D11), 20795–20808. https://doi.org/10.1029/91jd02212

1114 Intrieri, J. M., Shupe, M. D., Uttal, T., & McCarty, B. J. (2002). An annual cycle of Arctic cloud
1115 characteristics observed by radar and lidar at SHEBA. *Journal of Geophysical Research:*
1116 *Oceans*, *107*(10), SHE 5-1. https://doi.org/10.1029/2000jc000423

1117 Jackson, R. C., McFarquhar, G. M., Korolev, A. V., Earle, M. E., Liu, P. S. K., Lawson, R. P., et
1118 al. (2012). The dependence of ice microphysics on aerosol concentration in arctic mixed-phase
1119 stratus clouds during ISDAC and M-PACE. *Journal of Geophysical Research Atmospheres*,
1120 *117*(15). https://doi.org/10.1029/2012JD017668

1121 Jackson, R. C., Mcfarquhar, G. M., Stith, J., Beals, M., Shaw, R. A., Jensen, J., et al. (2014). An
1122 assessment of the impact of antishattering tips and artifact removal techniques on cloud ice size
1123 distributions measured by the 2D cloud probe. *Journal of Atmospheric and Oceanic Technology*,
1124 *31*(12), 2567–2590. https://doi.org/10.1175/JTECH-D-13-00239.1

1125 Jaczewski, A., & Malinowski, S. P. (2005). Spatial distribution of cloud droplets in a turbulent
1126 cloud-chamber flow. *Quarterly Journal of the Royal Meteorological Society*, *131*(609), 2047–
1127 2062. https://doi.org/10.1256/qj.04.65

1128 Järvinen, E., McCluskey, C. S., Waitz, F., Schnaiter, M., Bansemer, A., Bardeen, C. G., et al.
1129 (2022). Evidence for Secondary Ice Production in Southern Ocean Maritime Boundary Layer
1130 Clouds. *Journal of Geophysical Research: Atmospheres*, *127*(16), e2021JD036411.
1131 https://doi.org/10.1029/2021jd036411

1132 Jensen, J. B., & Nugent, A. D. (2017). Condensational growth of drops formed on giant sea-salt
1133 aerosol particles. *Journal of the Atmospheric Sciences*, *74*(3), 679–697.
1134 https://doi.org/10.1175/JAS-D-15-0370.1

1135 Jiang, Q., & Wang, S. (2012). Impact of Gravity Waves on Marine Stratocumulus Variability.
1136 *Journal of the Atmospheric Sciences*, *69*(12), 3633–3651. https://doi.org/10.1175/JAS-D-12-
1137 0135.1

Kay, J. E., Hillman, B. R., Klein, S. A., Zhang, Y., Medeiros, B., Pincus, R., et al. (2012). Exposing Global Cloud Biases in the Community Atmosphere Model (CAM) Using Satellite Observations and Their Corresponding Instrument Simulators. *Journal of Climate*, *25*(15), 5190–5207. https://doi.org/10.1175/JCLI-D-11-00469.1

Khanal, S., & Wang, Z. (2018). Uncertainties in MODIS-Based Cloud Liquid Water Path Retrievals at High Latitudes Due to Mixed-Phase Clouds and Cloud Top Height Inhomogeneity. *Journal of Geophysical Research: Atmospheres*, *123*(19), 11,154-11,172. https://doi.org/10.1029/2018JD028558

Kim, S., & Casper, R. (2013). Applications of convolution in image processing with MATLAB. *University of Washington*, 1–20.

Korolev, A., & Leisner, T. (2020). Review of experimental studies of secondary ice production. *Atmospheric Chemistry and Physics*, *20*(20), 11767–11797. https://doi.org/10.5194/acp-20-11767-2020

Korolev, A., Khain, A., Pinsky, M., & French, J. (2016). Theoretical study of mixing in liquid clouds-Part 1: Classical concepts. *Atmospheric Chemistry and Physics*, *16*(14), 9235–9254. https://doi.org/10.5194/acp-16-9235-2016

Kostinski, A. B., & Shaw, R. A. (2001). Scale-dependent droplet clustering in turbulent clouds. *Journal of Fluid Mechanics*, *434*, 389–398. https://doi.org/10.1017/S0022112001004001

Lamb, D., & Verlinde, J. (2011). *Physics and chemistry of clouds*. *Physics and Chemistry of Clouds*. Cambridge University Press. https://doi.org/10.1017/CBO9780511976377

Lance, S., Brock, C. A., Rogers, D., & Gordon, J. A. (2010). Water droplet calibration of the Cloud Droplet Probe (CDP) and in-flight performance in liquid, ice and mixed-phase clouds during ARCPAC. *Atmospheric Measurement Techniques*, *3*(6), 1683–1706. https://doi.org/10.5194/amt-3-1683-2010

Latham, J., & Reed, R. L. (1977). Laboratory studies of the effects of mixing on the evolution of cloud droplet spectra. *Quarterly Journal of the Royal Meteorological Society*, *103*(436), 297–306. https://doi.org/10.1002/qj.49710343607

Levin, E. J. T., DeMott, P. J., Suski, K. J., Boose, Y., Hill, T. C. J., McCluskey, C. S., et al. (2019). Characteristics of Ice Nucleating Particles in and Around California Winter Storms. *Journal of Geophysical Research: Atmospheres*, *124*(21), 11530–11551. https://doi.org/10.1029/2019JD030831

Li, J., Yi, Y., Minnis, P., Huang, J., Yan, H., Ma, Y., et al. (2011). Radiative effect differences between multi-layered and single-layer clouds derived from CERES, CALIPSO, and CloudSat data. *Journal of Quantitative Spectroscopy and Radiative Transfer*, *112*(2), 361–375. https://doi.org/10.1016/j.jqsrt.2010.10.006

Liu, Y., Key, J. R., Ackerman, S. A., Mace, G. G., & Zhang, Q. (2012). Arctic cloud macrophysical characteristics from CloudSat and CALIPSO. *Remote Sensing of Environment*, *124*, 159–173. https://doi.org/10.1016/j.rse.2012.05.006

Luo, Y., Xu, K.-M., Morrison, H., McFarquhar, G. M., Wang, Z., & Zhang, G. (2008). Multi-layer arctic mixed-phase clouds simulated by a cloud-resolving model: Comparison with ARM observations and sensitivity experiments. *Journal of Geophysical Research*, *113*(D12), D12208. https://doi.org/10.1029/2007JD009563

Matus, A. V., & L'Ecuyer, T. S. (2017). The role of cloud phase in Earth's radiation budget. *Journal of Geophysical Research: Atmospheres*, *122*(5), 2559–2578. https://doi.org/10.1002/2016JD025951

McCluskey, C. S., Hill, T. C. J., Humphries, R. S., Rauker, A. M., Moreau, S., Strutton, P. G., et al. (2018). Observations of Ice Nucleating Particles Over Southern Ocean Waters. *Geophysical Research Letters*, *45*(21), 11,989-11,997. https://doi.org/10.1029/2018GL079981

McCoy, D. T., Hartmann, D. L., Grosvenor, D. P., McCoy, D. T., Hartmann, D. L., & Grosvenor, D. P. (2014). Observed Southern Ocean Cloud Properties and Shortwave Reflection. Part I: Calculation of SW Flux from Observed Cloud Properties*. *Journal of Climate*, *27*(23), 8836–8857. https://doi.org/10.1175/JCLI-D-14-00287.1

McCoy, I. L., Bretherton, C. S., Wood, R., Twohy, C. H., Gettelman, A., Bardeen, C. G., & Toohey, D. W. (2021). Influences of Recent Particle Formation on Southern Ocean Aerosol Variability and Low Cloud Properties. *Journal of Geophysical Research: Atmospheres*, *126*(8), e2020JD033529. https://doi.org/10.1029/2020JD033529

McFarquhar, G., Zhang, G., Poellot, M. R., Kok, G. L., McCoy, R., Tooman, T., et al. (2007). Ice properties of single-layer stratocumulus during the Mixed-Phase Arctic Cloud Experiment: 1. Observations. *Journal of Geophysical Research*, *112*(D24), D24201. https://doi.org/10.1029/2007JD008633

McFarquhar, G. M., Finlon, J. A., Stechman, D. M., Wu, W., & Jackson, Robert M. Freer, M. (2018). University of Illinois/Oklahoma Optical Array Probe (OAP) Processing Software. Version 3.1.4. Zenodo. https://doi.org/doi:http://doi.org/10.5281/

McFarquhar, Greg M. (2004). The effect of raindrop clustering on collision-induced break-up of raindrops. *Quarterly Journal of the Royal Meteorological Society*, *130*(601), 2169–2190. https://doi.org/10.1256/qj.03.98

McFarquhar, Greg M., Baumgardner, D., Bansemer, A., Abel, S. J., Crosier, J., French, J., et al. (2017). Processing of Ice Cloud In Situ Data Collected by Bulk Water, Scattering, and Imaging Probes: Fundamentals, Uncertainties, and Efforts toward Consistency. *Meteorological Monographs*, *58*, 11.1-11.33. https://doi.org/10.1175/amsmonographs-d-16-0007.1

McFarquhar, Greg M., Bretherton, C., Marchand, R., Protat, A., DeMott, P. J., Alexander, S. P., et al. (2021). Observations of clouds, aerosols, precipitation, and surface radiation over the Southern Ocean: An overview of CAPRICORN, MARCUS, MICRE and SOCRATES. *Bulletin*

1211 *of the American Meteorological Society*, *102*(4), E894–E928. https://doi.org/10.1175/bams-d-20-
1212 0132.1

1213 Mioche, G., Jourdan, O., Delanoë, J., Gourbeyre, C., Febvre, G., Dupuy, R., et al. (2017).
1214 Vertical distribution of microphysical properties of Arctic springtime low-level mixed-phase
1215 clouds over the Greenland and Norwegian seas. *Atmospheric Chemistry and Physics*, *17*(20),
1216 12845–12869. https://doi.org/10.5194/acp-17-12845-2017

1217 Mossop, S. C. (1956). Sublimation nuclei. *Proceedings of the Physical Society. Section B*, *69*(2),
1218 161–164. https://doi.org/10.1088/0370-1301/69/2/305

1219 Murphy, D. M., & Koop, T. (2005). Review of the vapour pressures of ice and supercooled water
1220 for atmospheric applications. *Quarterly Journal of the Royal Meteorological Society*, *131*(608),
1221 1539–1565. https://doi.org/10.1256/qj.04.94

1222 Naud, C. M., Booth, J. F., & Del Genio, A. D. (2014). Evaluation of ERA-Interim and MERRA
1223 cloudiness in the southern ocean. *Journal of Climate*, *27*(5), 2109–2124.
1224 https://doi.org/10.1175/JCLI-D-13-00432.1

1225 Paluch, I. R. (1986). Mixing and the cloud droplet size spectrum: generalizations from the
1226 CCOPE data. *Journal of the Atmospheric Sciences*, *43*(18), 1984–1993.
1227 https://doi.org/10.1175/1520-0469(1986)043<1984:MATCDS>2.0.CO;2

1228 Paluch, I. R., & Knight, C. A. (1984). Mixing and the evolution of cloud droplet size spectra in a
1229 vigorous continental cumulus. *Journal of the Atmospheric Sciences*, *41*(11), 1801–1815.
1230 https://doi.org/10.1175/1520-0469(1984)041<1801:MATEOC>2.0.CO;2

1231 Petty, G. W. (Grant W. (2006). *A first course in atmospheric radiation*. Sundog Pub. Retrieved
1232 from https://sundogpublishingstore.myshopify.com/products/a-first-course-in-atmospheric-
1233 radiation-g-w-petty

1234 Pruppacher, H. R., & Klett, J. D. (1996). *Microphysics of Clouds and Precipitation*. Springer
1235 Netherlands.

1236 Rahn, D. A., & Garreaud, R. (2010). Marine boundary layer over the subtropical southeast
1237 Pacific during VOCALS-REx-Part 1: Mean structure and diurnal cycle. *Atmospheric Chemistry*
1238 *and Physics*, *10*(10), 4491–4506. https://doi.org/10.5194/acp-10-4491-2010

1239 Rauber, R. M., Hu, H., Dominguez, F., Nesbitt, S. W., McFarquhar, G. M., Zaremba, T. J., &
1240 Finlon, J. A. (2020). Structure of an Atmospheric River Over Australia and the Southern Ocean.
1241 Part I: Tropical and Midlatitude Water Vapor Fluxes. *Journal of Geophysical Research:*
1242 *Atmospheres*, *125*(18), e2020JD032513. https://doi.org/10.1029/2020JD032513

1243 Riedi, J., Marchant, B., Platnick, S., Baum, B. A., Thieuleux, F., Oudard, C., et al. (2010). Cloud
1244 thermodynamic phase inferred from merged POLDER and MODIS data. *Atmospheric Chemistry*
1245 *and Physics*, *10*(23), 11851–11865. https://doi.org/10.5194/acp-10-11851-2010

1246   Roberts, G. C., & Nenes, A. (2005). A Continuous-Flow Streamwise Thermal-Gradient CCN
1247   Chamber for Atmospheric Measurements. *Aerosol Science and Technology*, *39*(3), 206–221.
1248   https://doi.org/10.1080/027868290913988

1249   Sanchez, K. J., Russell, L. M., Modini, R. L., Frossard, A. A., Ahlm, L., Corrigan, C. E., et al.
1250   (2016). Meteorological and aerosol effects on marine cloud microphysical properties. *Journal of*
1251   *Geophysical Research: Atmospheres*, *121*(8), 4142–4161. https://doi.org/10.1002/2015JD024595

1252   Sanchez, Kevin J., Roberts, G. C., Saliba, G., Russell, L. M., Twohy, C., Reeves, M. J., et al.
1253   (2021). Measurement report: Cloud processes and the transport of biological emissions affect
1254   southern ocean particle and cloud condensation nuclei concentrations. *Atmospheric Chemistry*
1255   *and Physics*, *21*(5), 3427–3446. https://doi.org/10.5194/acp-21-3427-2021

1256   Savitzky, A., & Golay, M. J. E. (1964). Smoothing and Differentiation of Data by Simplified
1257   Least Squares Procedures. *Analytical Chemistry*, *36*(8), 1627–1639.
1258   https://doi.org/10.1021/ac60214a047

1259   Schima, J., McFarquhar, G., Romatschke, U., Vivekanandan, J., D'Alessandro, J., Haggerty, J.,
1260   et al. (2022). Characterization of Southern Ocean Boundary Layer Clouds Using Airborne Radar,
1261   Lidar, and In-situ Cloud Data: Results from SOCRATES. *Journal of Geophysical Research:*
1262   *Atmospheres*.

1263   Seidel, D. J., Zhang, Y., Beljaars, A., Golaz, J.-C., Jacobson, A. R., & Medeiros, B. (2012).
1264   Climatology of the planetary boundary layer over the continental United States and Europe.
1265   *Journal of Geophysical Research: Atmospheres*, *117*(D17).
1266   https://doi.org/10.1029/2012JD018143

1267   Shaw, R. A., Kostinski, A. B., & Larsen, M. L. (2002). Towards quantifying droplet clustering in
1268   clouds. *Quarterly Journal of the Royal Meteorological Society*, *128*(582), 1043–1057.
1269   https://doi.org/10.1256/003590002320373193

1270   Shaw, Raymond A., Reade, W. C., Collins, L. R., & Verlinde, J. (1998). Preferential
1271   concentration of cloud droplets by turbulence: Effects on the early evolution of cumulus cloud
1272   droplet spectra. *Journal of the Atmospheric Sciences*, *55*(11), 1965–1976.
1273   https://doi.org/10.1175/1520-0469(1998)055<1965:PCOCDB>2.0.CO;2

1274   Small, J. D., & Chuang, P. Y. (2008). New observations of precipitation initiation in warm
1275   cumulus clouds. *Journal of the Atmospheric Sciences*, *65*(9), 2972–2982.
1276   https://doi.org/10.1175/2008JAS2600.1

1277   Solomon, A., Shupe, M. D., Persson, P. O. G., & Morrison, H. (2011). Moisture and dynamical
1278   interactions maintaining decoupled Arctic mixed-phase stratocumulus in the presence of a
1279   humidity inversion. *Atmospheric Chemistry and Physics*, *11*(19), 10127–10148.
1280   https://doi.org/10.5194/acp-11-10127-2011

1281   Stith, J. L., Ramanathan, V., Cooper, W. A., Roberts, G. C., DeMott, P. J., Carmichael, G., et al.
1282   (2009). An overview of aircraft observations from the Pacific Dust Experiment campaign.
1283   *Journal of Geophysical Research*, *114*(D5), D05207. https://doi.org/10.1029/2008JD010924

Trenberth, K. E., & Fasullo, J. T. (2010). Simulation of Present-Day and Twenty-First-Century Energy Budgets of the Southern Oceans. *Journal of Climate*, *23*(2), 440–454. https://doi.org/10.1175/2009JCLI3152.1

Tsay, S. C., & Jayaweera, K. (1984). Physical characteristics of Arctic stratus clouds. *Journal of Climate & Applied Meteorology*, *23*(4), 584–596. https://doi.org/10.1175/1520-0450(1984)023<0584:PCOASC>2.0.CO;2

Twohy, C. H., McMeeking, G. R., DeMott, P. J., McCluskey, C. S., Hill, T. C. J., Burrows, S. M., et al. (2016). Abundance of fluorescent biological aerosol particles at temperatures conducive to the formation of mixed-phase and cirrus clouds. *Atmospheric Chemistry and Physics*, *16*(13), 8205–8225. https://doi.org/10.5194/acp-16-8205-2016

UCAR/NCAR—Earth Observing Laboratory. (2018). NSF/NCAR GV HIAPER raw 2D-S imagery. Version 1.0 [Dataset]. *UCAR/NCAREarth*. https://doi.org/https://doi.org/10.26023/8HMG-WQP3-XA0X

UCAR/NCAR—Earth Observing Laboratory. (2022). SOCRATES: Low rate (LRT - 1 sps) navigation, state parameter, and microphysics flight-level data. Version 1.4 [Dataset]. *UCAR/NCAREarth*. https://doi.org/10.5065/D6M32TM9

Verlinde, J., Rambukkange, M. P., Clothiaux, E. E., McFarquhar, G. M., & Eloranta, E. W. (2013). Arctic multilayered, mixed-phase cloud processes revealed in millimeter-wave cloud radar Doppler spectra. *Journal of Geophysical Research: Atmospheres*, *118*(23), 13,199-13,213. https://doi.org/10.1002/2013JD020183

Vivekanandan, J., Ellis, S., Tsai, P., Loew, E., Lee, W. C., Emmett, J., et al. (2015). A wing pod-based millimeter wavelength airborne cloud radar A wing pod-based millimeter wavelength airborne cloud radar A wing pod-based millimeter wavelength airborne cloud radar. *Geosci. Instrum. Method. Data Syst. Discuss*, *5*, 117–159. https://doi.org/10.5194/gid-5-117-2015

Vogelezang, D. H. P., & Holtslag, A. A. M. (1996). Evaluation and model impacts of alternative boundary-layer height formulations. *Boundary-Layer Meteorology*, *81*(3), 245–269. https://doi.org/10.1007/BF02430331

Wang, Y., McFarquhar, G. M., Rauber, R. M., Zhao, C., Wu, W., Finlon, J. A., et al. (2020). Microphysical Properties of Generating Cells Over the Southern Ocean: Results From SOCRATES. *Journal of Geophysical Research: Atmospheres*, *125*(13). https://doi.org/10.1029/2019JD032237

Wang, Z., Mora Ramirez, M., Dadashazar, H., MacDonald, A. B., Crosbie, E., Bates, K. H., et al. (2016). Contrasting cloud composition between coupled and decoupled marine boundary layer clouds. *Journal of Geophysical Research: Atmospheres*, *121*(19), 11,679-11,691. https://doi.org/10.1002/2016JD025695

Wu, W., & McFarquhar, G. M. (2019). NSF/NCAR GV Hiaper fast 2DS particle size distribution (psd) product data. Version 1.1. UCAR/NCAR-Earth Observing Laboratory [dataset]. https://doi.org/10.26023/8hmg-wqp3-xa0x

1322 Yang, C. A., Diao, M., Gettelman, A., Zhang, K., Sun, J., McFarquhar, G., & Wu, W. (2021). Ice
1323 and Supercooled Liquid Water Distributions Over the Southern Ocean Based on In Situ
1324 Observations and Climate Model Simulations. *Journal of Geophysical Research: Atmospheres*,
1325 *126*(24), e2021JD036045. https://doi.org/10.1029/2021JD036045

1326 Zondlo, M. A., Paige, M. E., Massick, S. M., & Silver, J. A. (2010). Vertical cavity laser
1327 hygrometer for the National Science Foundation Gulfstream-V aircraft. *Journal of Geophysical*
1328 *Research*, *115*(D20), D20309. https://doi.org/10.1029/2010JD014445
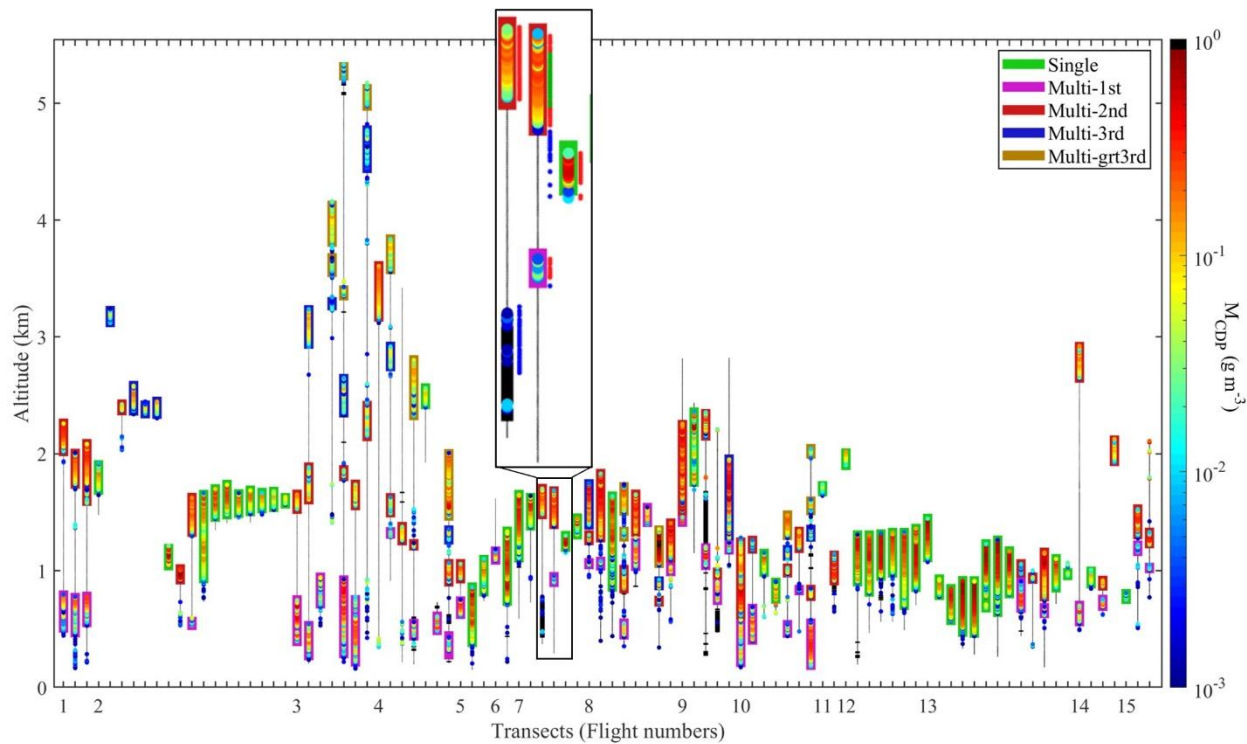
1329

1330 Figure 1: Vertical profiles of M_{CDP} from select sawtooths that meet criteria described in Section

1331 2. Profiles are only shown for transects where the highest and lowest altitude samples of each

1332 transect are considered clear-sky. Colored circles show M_{CDP} where $M_{CDP} > 0.001$ g m^{-3}. Solid

1333 black lines show the vertical extent of each transect. Black shaded regions represent samples

1334 where $M_{2DS} > 0.01$ g m^{-3} and $M_{CDP} < 0.001$ g m^{-3}. Red, green and blue markers to the right of the

1335 transects in the magnified panel indicate liquid, mixed and ice phase samples, respectively. Phase

1336   markers are only shown for temperatures less than 0°C. Transects are from research flights

1337   which incrementally follow the flight numbers in the x-axis (e.g., all transects greater than or

1338   equal to 2 and less than 3 on the x-axis are from RF02). Note that cloud layers are slightly

1339   enlarged in order to encapsulate enlarged M_{CDP} markers.
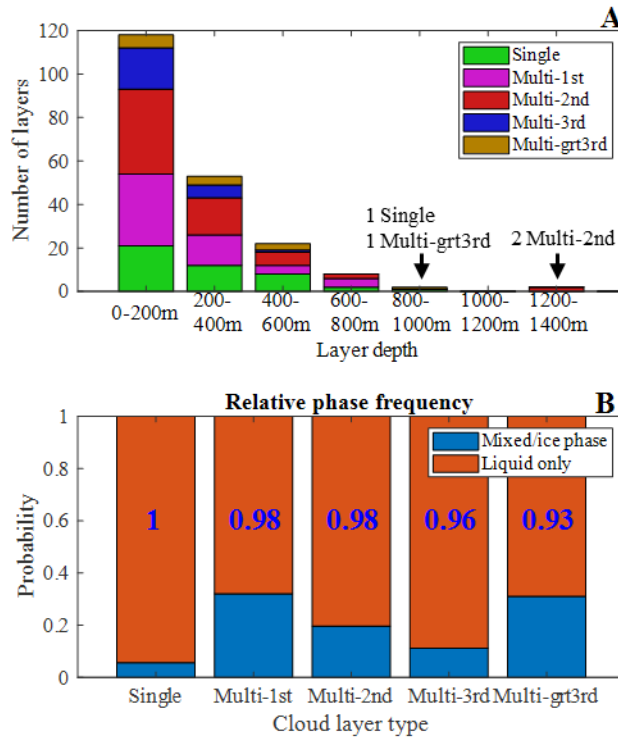
1340   Figure 2: A) A bar chart showing the number of cloud layers with given depth, sorted according

1341   to different cloud layer types. B) Relative cloud phase frequency shown for different cloud layer

1342   types. Results in B) are only shown at temperatures less than 0°C. The blue numbers are relative

1343   frequencies of the mixed phase to all ice-containing samples (mixed and ice phase). Results are

1344   only shown for sawtooths.
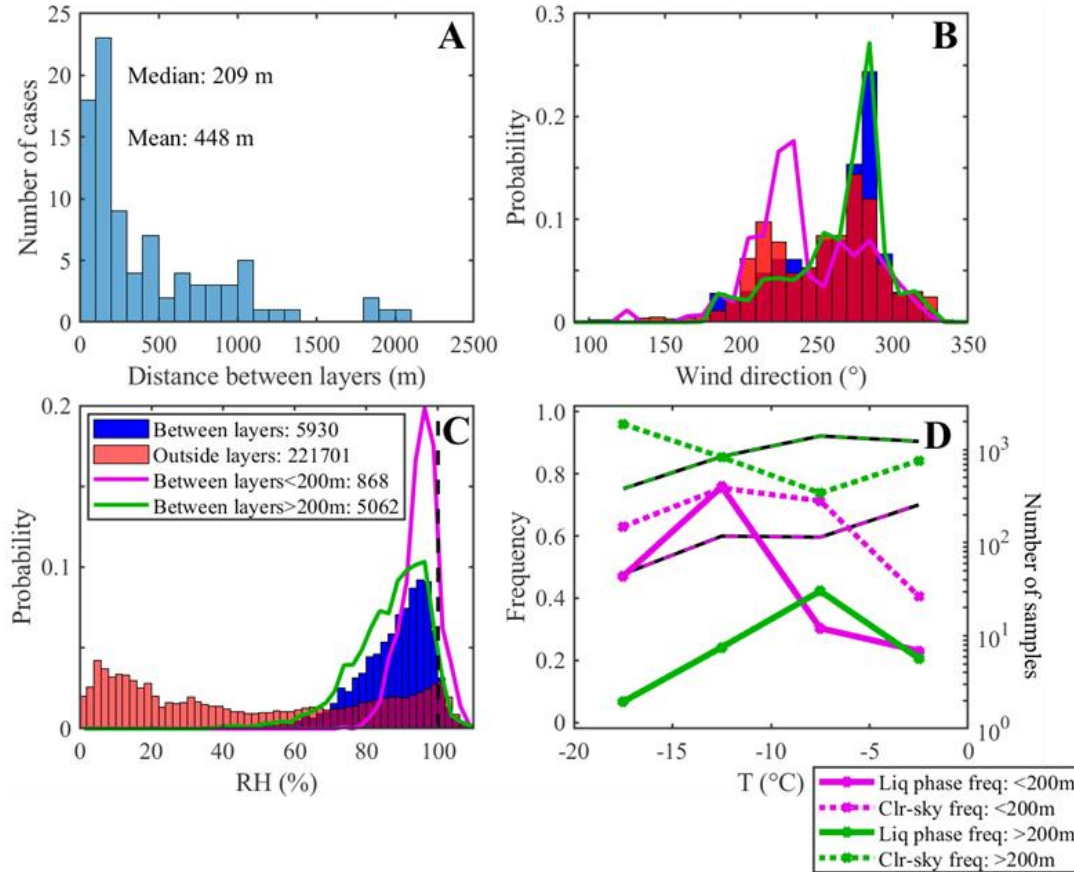
Figure 3: A) Histogram of depth lengths in between cloud layers. The mean and median depth lengths are shown in the panel. B) Normalized frequency distributions of wind direction for different conditions. The legend in C applies to subsets here, and the sample size of the subsets is provided in the legend. The purple (green) line represents the distribution of samples within cloud layers where the depth is less than (more than) 200 m. The outside layer includes all samples from the northbound portion of the research flights, excluding samples between and within cloud layers, as well as samples lower than the lowest altitude of samples within layers (< 450 m). C) Normalized frequency distributions of relative humidity. Subsets of distributions are similar to those in B. D) Liquid phase (solid line) and clear-sky (dashed line) relative frequencies

of samples in between layers binned in 5°C temperature intervals. Results are similarly restricted

to depths less than and greater than 200 m as in B&C. The black and purple (green) dashed line

shows the number of samples for depths less (greater) than 200 m (right ordinate).
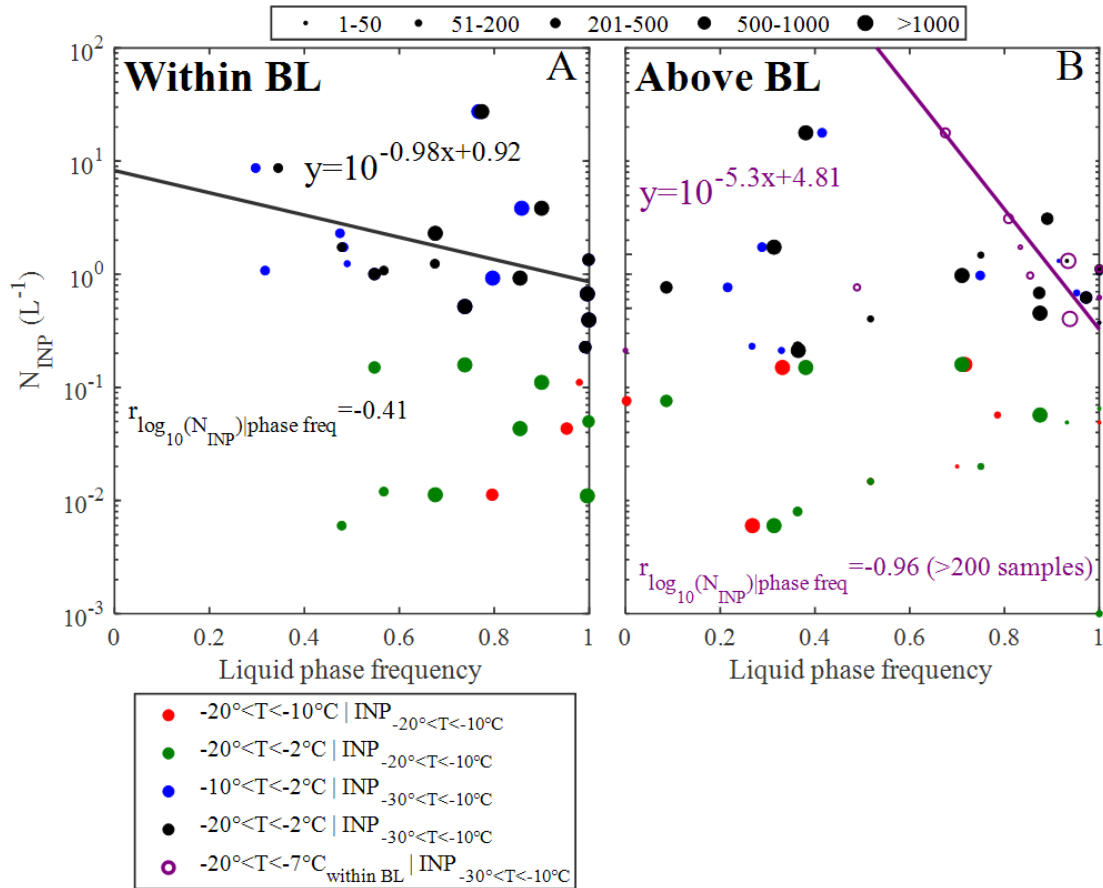
Figure 4: Scatterplots of N_{INP} related to liquid phase frequency (i.e., the frequency of liquid

phase samples relative to all in-cloud samples) for samples within the boundary layer (A) and

above the boundary layer (B). Samples are taken within the interpolated INP sample areas as

described in the text. Different colored markers show liquid phase frequencies taken within

specified temperature ranges compared with N_{INP} having different ranges of activation

temperatures. The purple circles compare phase frequencies within the boundary layer to N_{INP}

above the boundary layer using the above boundary layer interpolated area. Best fit lines and

1353   correlations correspond to the respective phase frequency and INP activation temperature ranges.

1354   The size of the data points represents the number of in-cloud samples associated with a given

1355   data point (i.e., the number of in-cloud samples within a specified temperature range located

1356   within a given interpolated sample area).
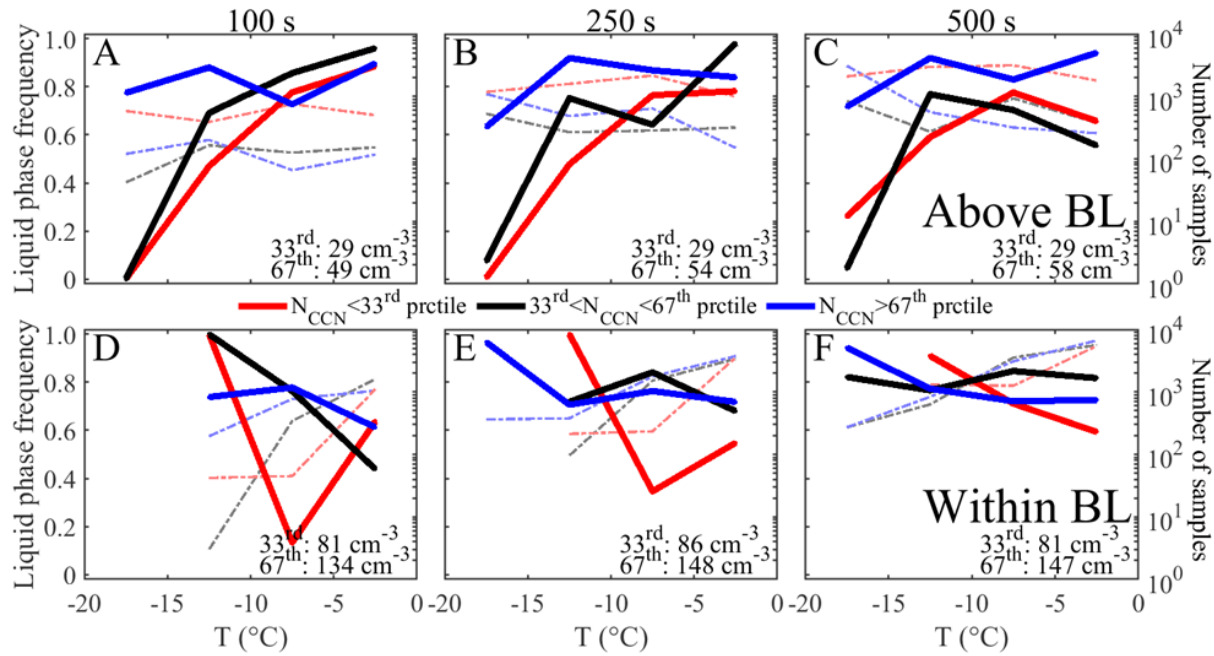
1357

1358   Figure 5: Liquid phase frequencies within 5°C temperature bins above (A–C) and within (D–F)

1359   the boundary layer for different N_{CCN} terciles. A "background CCN concentration" (N_{CCN}) is

1360   determined for each in-cloud sample by averaging the CCN concentration measurements over

1361   the clear-sky samples within a window of ±n seconds from each in-cloud sample. Results are

1362   shown for different moving window sizes, which are shown overlying each respective column.

1363   Temperatures are from the location of the respective in-cloud samples. Frequencies are

1364   determined for different ranges of average N_{CCN} (shown by the colored lines). Average N_{CCN}

1365   terciles are calculated within the respective temperature bins, whereas terciles calculated over the

57

1366　entire temperature range are included in the respective panels. The number of in-cloud samples

1367　are denoted by the dotted-dashed lines.

1368
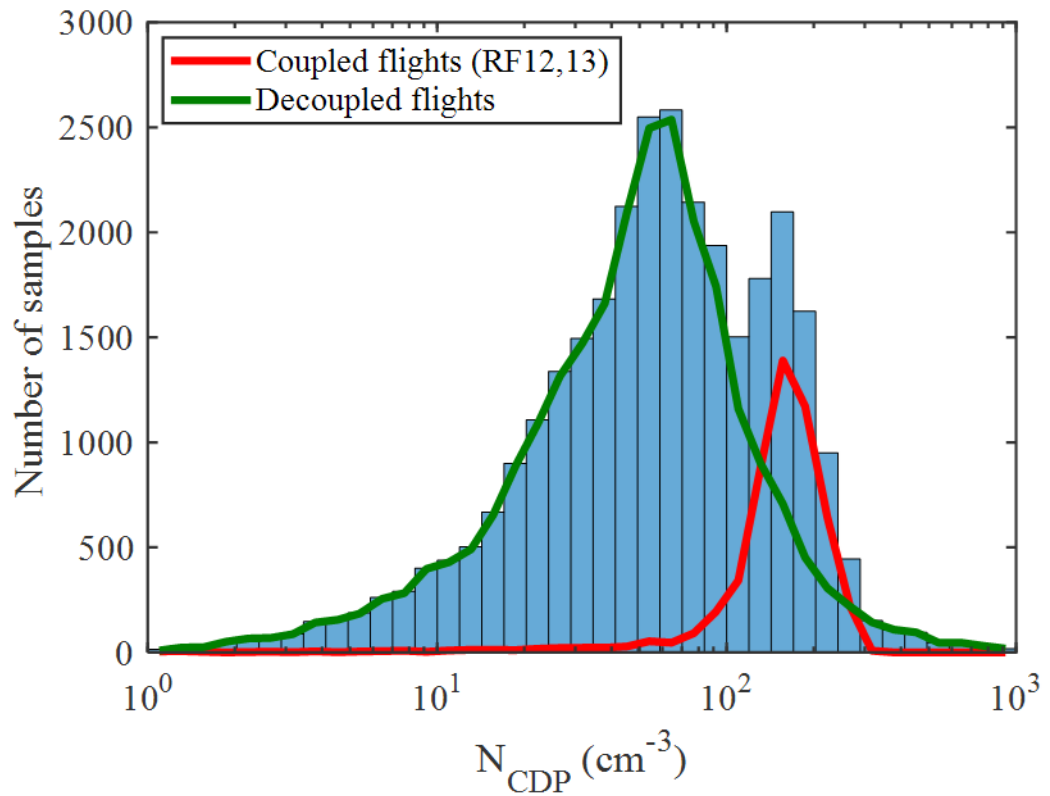
1369

1370

1371　Figure 6: Frequency distribution of N_{CDP} for in-cloud conditions for all flights (blue bars). Green

1372　and red lines show distributions of N_{CDP} for decoupled and coupled environments, respectively.

1373　Results here include level periods and sawtooths.
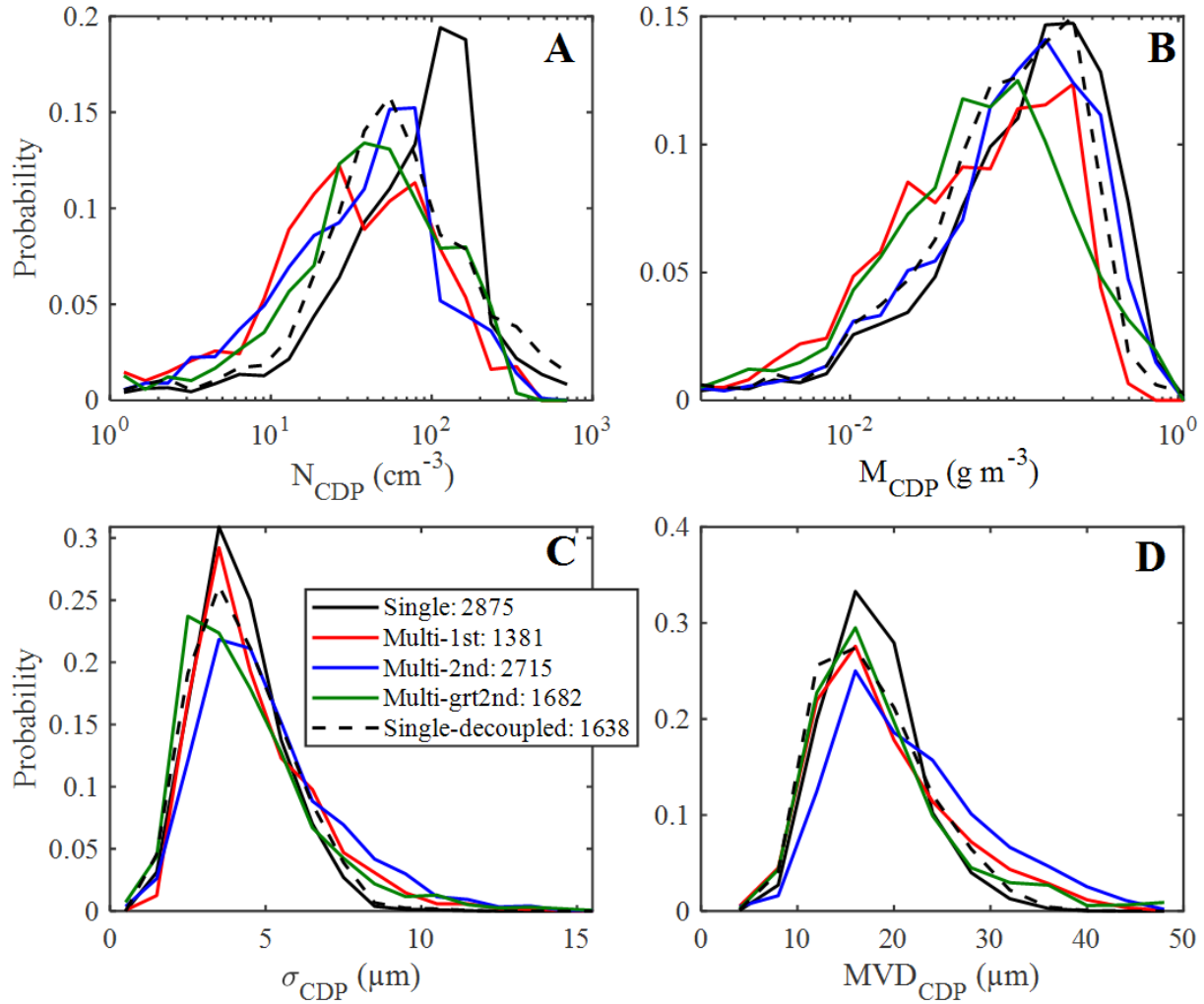
Figure 7: Normalized probability distributions of N_{CDP} (A), M_{CDP} (B), σ_{CDP} (C) and MVD_{CDP} (D) for different cloud layer types. The black solid and dashed lines show all single-layer samples and single-layer samples from decoupled environments, respectively. The number of samples for each layer type is shown in the legend. Results are only shown for sawtooths.
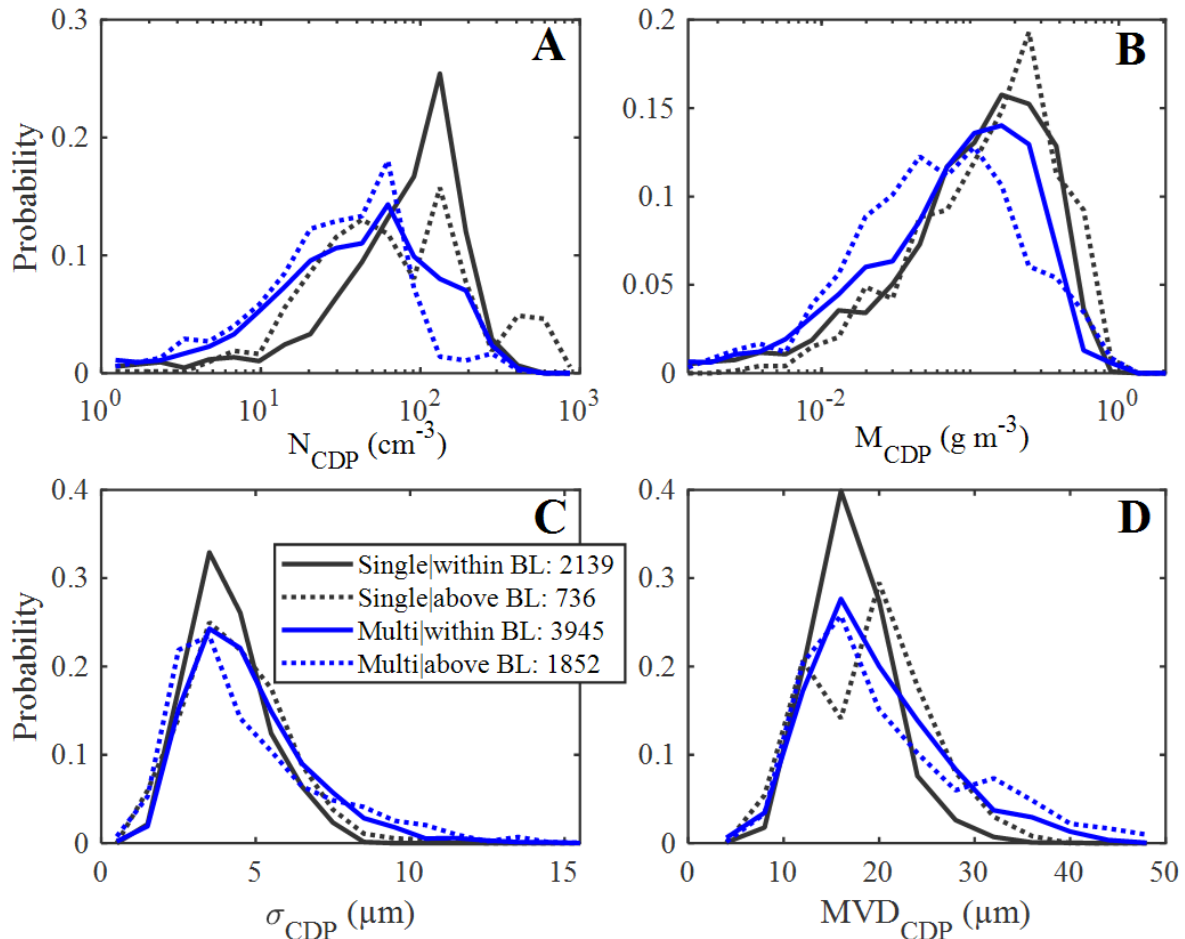
Figure 8: Similar to Figure 7, except single- and multi-layer cloud properties are separately evaluated for samples above the boundary layer and within the boundary layer.
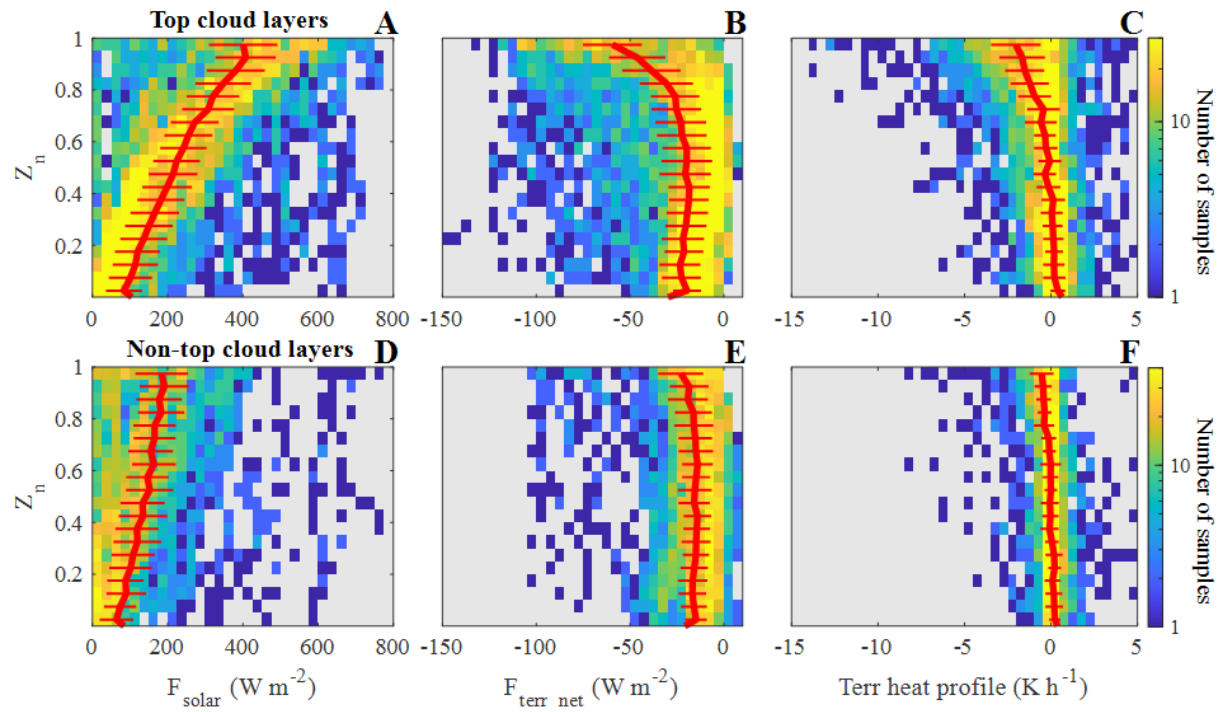
Figure 9: Joint histograms showing the frequency of downwelling solar irradiance (F_{solar}; A,D), net terrestrial irradiance (F_{terr_net}; B,E) and associated heating profiles from terrestrial irradiance (C,F) as a function of z_n for layers including single-layer and the highest layer of multi-layer clouds (top cloud layers; A, B, C) and for underlying cloud layers (non-top cloud layers; D, E, F). Vertical red lines show average irradiance and heating rates and horizontal lines denote standard deviations.
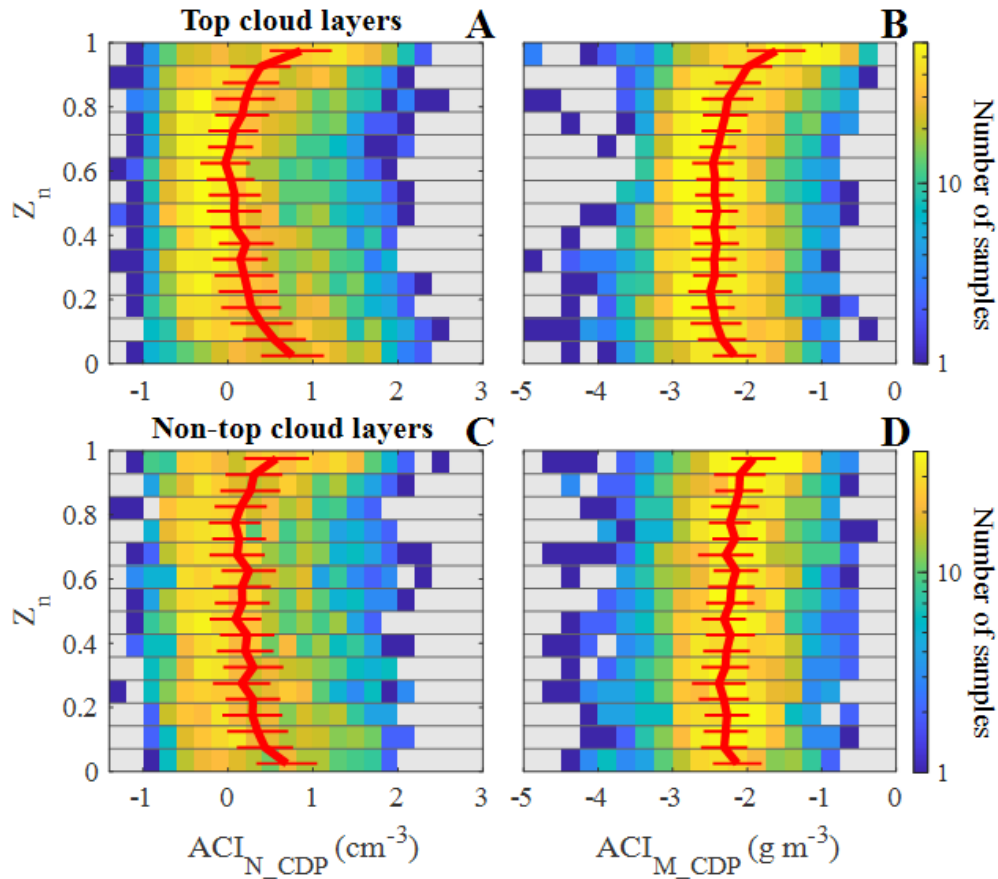
Figure 10: Joint histograms shown with ACI_{N_CDP} (A,C) and ACI_{M_CDP} (B,D). Unlike Figure 9, histograms are normalized over respective z_n intervals. The red vertical lines show average ACI_{N_CDP} and ACI_{M_CDP} and the horizontal lines denote standard deviations.
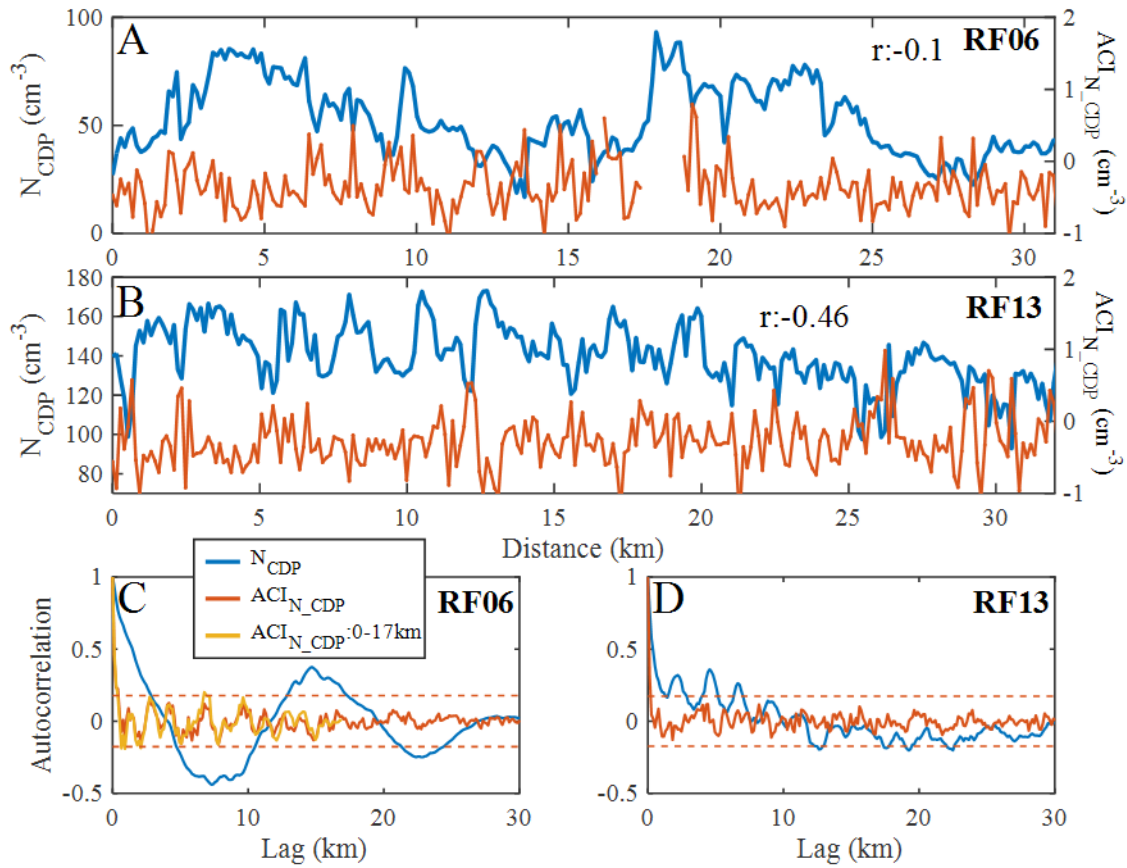
Figure 11: Two time series of level legs taken at cloud top showing N_{CDP} (blue) and ACI_{N_CDP} (red) from RF06 (01:47:00 to 01:51:55 UTC; A) and RF13 (02:19:00 to 02:24:00 UTC; B). Correlations are included in the respective panels. Autocorrelations of N_{CDP} and ACI_{N_CDP} are shown for RF06 (C) and RF13 (D). Bands for rejection testing each autocorrelation=0 under the assumption of white noise are shown as dashed lines, which are provided at the 95th percentiles. Autocorrelations are determined for flight data interpolated onto a 1D grid with a constant incrementally increasing distance (lag) of 130 m, based on the average flight speed for both cases (~130 m s^{-1}). The autocorrelation of ACI_{N_CDP} from 0–17 km is also provided for RF06, due to missing data from ~17.5–19 km (missing data is also observed at ~16 km, but the interpolation method captures the fine scale variability).
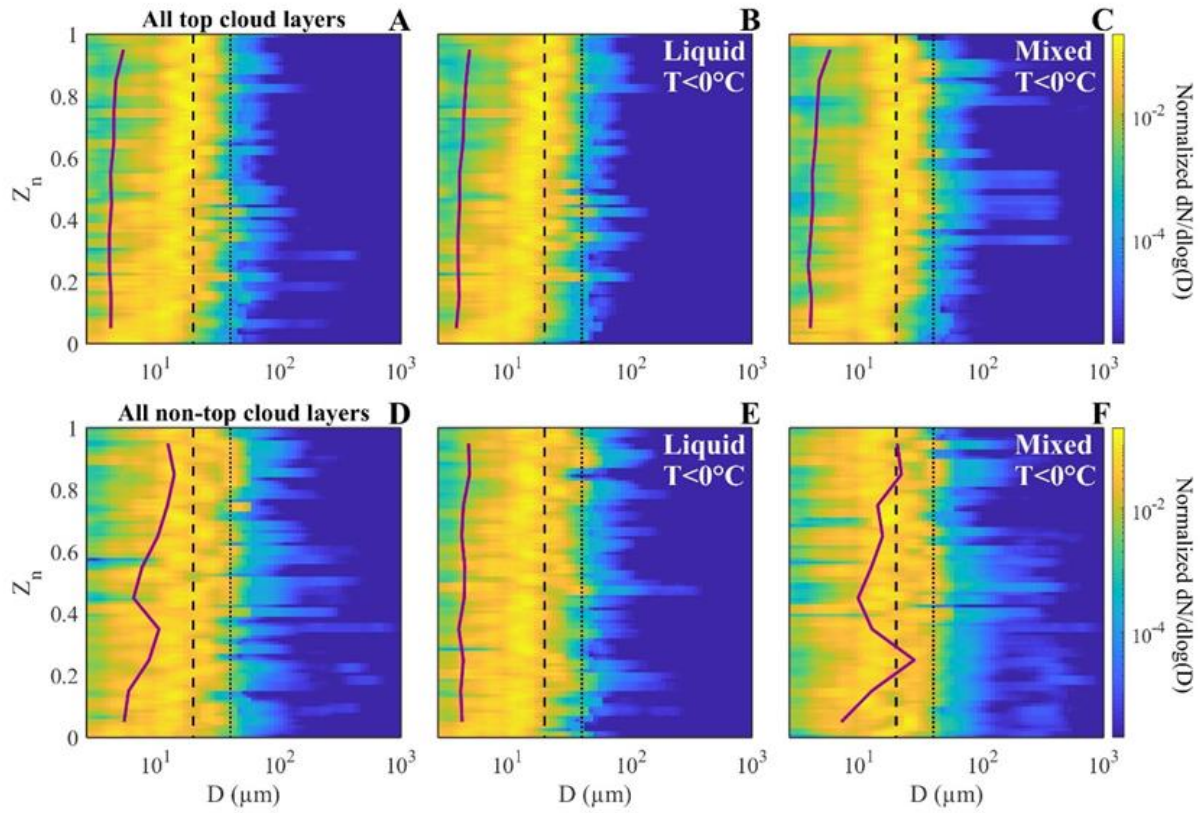
Figure 12: Normalized size distribution functions combining CDP and 2DS observations are averaged over z_n, using an image smoothing method outlined in the text. The top (bottom) row shows results for top (non-top) cloud layers. Results are shown for all in-cloud samples in the left column (A,D), liquid phase samples at temperatures less than 0°C in the middle column (B,E) and for mixed phase samples in the right column (C,F). Purple lines show the average standard deviation of particle size over the entire size distributions, applied prior to the convolution. The dashed and dotted lines correspond with D=20 μm and D=40 μm, respectively.
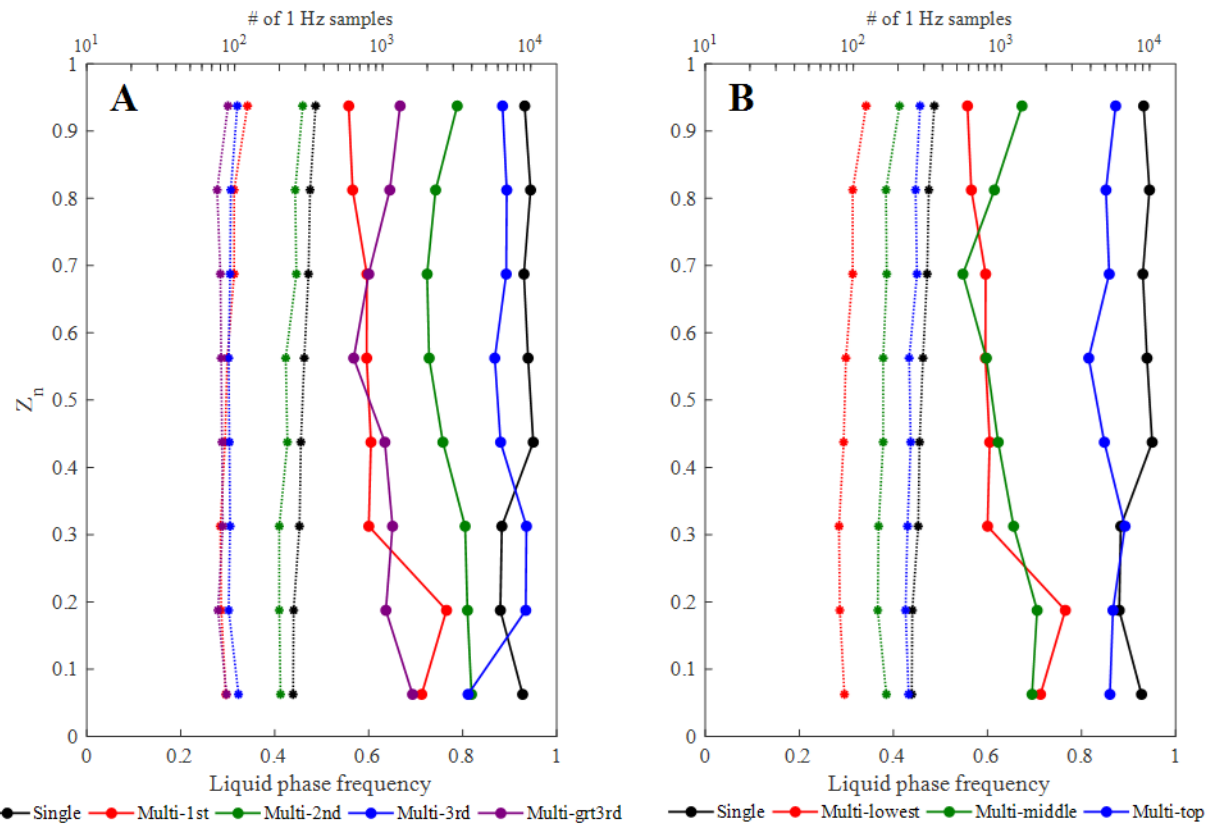
Figure 13: Cloud phase frequency as a function of z_n (solid lines) colored according to the cloud layer for single-layer and multi-layer clouds, where ordering of multi-layer height is characterized by incremental order from the lowest layer (A) and by whether layers are the lowest, highest, or in-between layer (B). Dotted lines show the number of samples for respective cloud layers following the top abscissa. Results are restricted to temperatures less than 0°C.
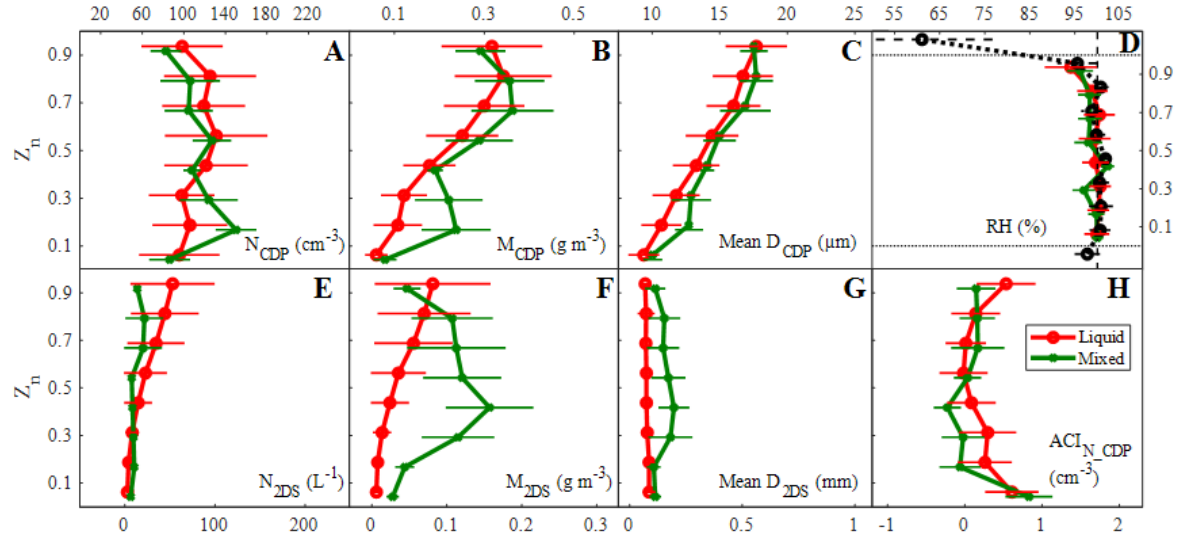
1418

Figure 14: Averaged N_{CDP} (A), M_{CDP} (B), Mean D_{CDP} (C), RH (D), N_{2DS} (E), M_{2DS} (F), Mean D_{2DS} (G) and ACI_{N_CDP} (H) as function of z_n for single-layer cloud regimes. Horizontal lines are standard deviations. Results are shown for liquid phase samples with the red lines and mixed phase samples with the green lines. Properties are averaged within z_n bin sizes of 0.125. All panels show results for z_n between 0 and 1 except for RH (D), which includes additional bins above and below the cloud (dashed lines). Black circles in RH denote clear-sky samples. Note error bars for the liquid phase in G are smaller than most of the data points.

1426
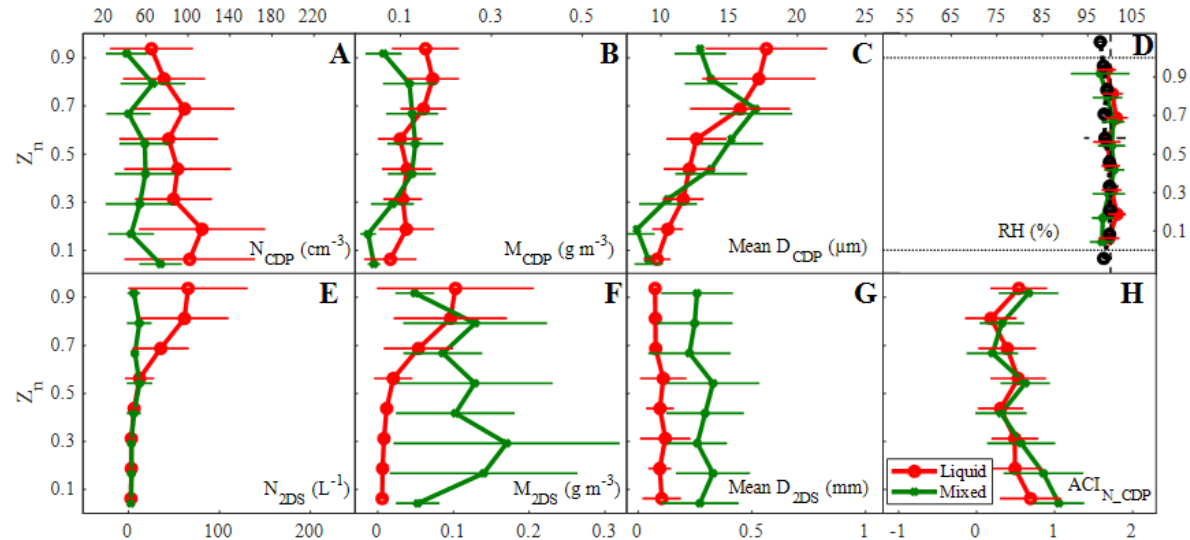
1427

1428　　Figure 15: Similar to Figure 14 except for the lowest layer of multi-layer clouds.
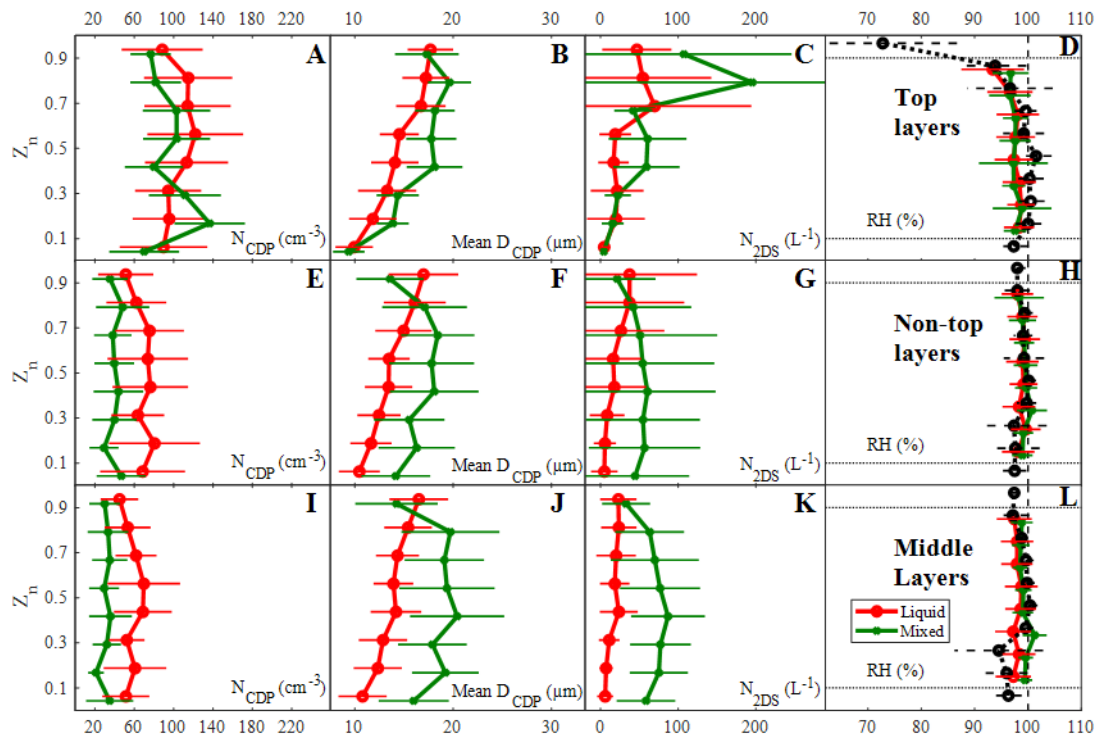
1429

Figure 16: Similar to Figure 14&15 except results are shown for the top cloud layers (A–D),

non-top cloud layers (E–H) and for all cloud layers enclosed within the lowest and highest cloud

layers of multi-layer clouds (I–L). Unlike Figure 14&15, results here are only shown for N_{CDP}

(A,E,I), Mean D_{CDP} (B,F,J), N_{2DS} (C,G,K) and RH (D,H,L).

1434   Supplementary material:
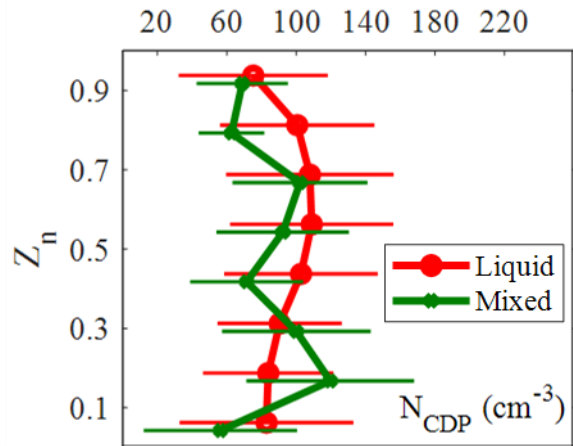
1435

1436   Figure A: Vertical profile of average N_{CDP} similar to Figure 14–16, except shown for the highest

1437   cloud layer of multi-layer clouds.
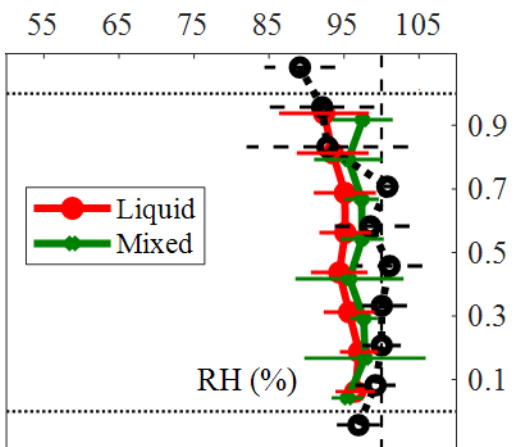
1438

1439   Figure B: Vertical profile of average RH similar to Figure 14–16, except shown for the highest

1440   cloud layer of multi-layer clouds.